# Synthetic natural gas production in a 1 kW reactor using Ni-Ce/$Al_2O_3$ and Ru-Ce/$Al_2O_3$: kinetics, catalyst degradation and process design

Manuel Bailera[a,b*], Pilar Lisbona[b], Begoña Peña[b], Andreina Alarcón[c,d], Jordi Guilera[c,e], Jorge Perpiñán[b], Luis M. Romeo[b]

[a] *Graduate School of Creative Science and Engineering, Waseda University, Okubo, Shinjuku-ku, Tokyo, 169-8555 Japan*
[b] *Escuela de Ingeniería y Arquitectura. Universidad de Zaragoza, Campus Río Ebro, María de Luna 3, 50018, Zaragoza, Spain*
[c] *Catalonia Institute for Energy Research (IREC), Jardins de les Dones de Negre 1, 08930 Sant Adrià de Besòs, Spain*
[d] *Escuela Superior Politécnica del Litoral (ESPOL), Facultad de Ingeniería en Ciencias de la Tierra, Campus Gustavo Galindo Km.30.5 Vía Perimetral, P.O. Box 09-01-5863, Guayaquil, Ecuador.*
*e Department of Chemical Engineering and Analytical Chemistry, University of Barcelona, Barcelona 08028, Spain*
**Corresponding author*

**Abstract:**

Nickel and ruthenium promoted by ceria were compared as catalyst active phase for the production of synthetic natural gas in a 1 kW fixed-bed reactor (49 cm in length and 3 cm in diameter). Both catalysts were tested in a broad range of conditions: 250 – 450 ºC, 8000 – 16000 $h^{-1}$ GHSV, 3.5 – 5.5 $H_2/CO_2$ ratio, and atmospheric pressure. The Ni-based catalyst presented higher $CO_2$ conversion and lower reduction of BET area and metal dispersion after utilization. Two kinetic models were elaborated according to the performance of the catalysts in this reactor. The minimum mean squared error between the kinetic model and experiments was 3.0% for the Ru-based catalyst and 1.4% for the Ni-based catalyst. The kinetic model of the Ni-based catalyst was implemented in Aspen Plus to evaluate potential methanation plant designs. The simulation minimized the amount of catalyst required to reach 95vol.% of $CH_4$, within proper technical limits (GHSV $\leq$ 5000 $h^{-1}$ and temperature $\geq$ 300 ºC). The 3-reactor plant was the most adequate configuration. The total catalyst mass was 3.26 kg per kg/h of SNG, the heat removed from the reactors was 10.8 MJ/$kg_{SNG}$, and the preheating necessity was 4.90 MJ/$kg_{SNG}$. The electrolysis energy consumption was 86.4 MJ/$kg_{SNG}$.

**Keywords:**

Power-to-Gas; hydrogen; methanation; synthetic natural gas; catalyst

# 1. Introduction

The massive penetration of renewable energy resources in the energy system, as well as the development of large scale energy storage systems, is essential to achieve global emissions targets [1]. Different technologies are currently in operation and others have been proposed to overcome the current drawbacks of energy storage technologies. Among them, Power to Gas has received attention in the recent years [2,3]. Power to Gas includes all those technological concepts that convert renewable electricity into gaseous fuel by including an electrolysis stage [4]. Considering the benefits and drawbacks of the different synthetic fuels that can be obtained, Power to Methane is one of the most versatile options thanks to the possibility of storing and distributing the product (methane) through the natural gas network [5–7]. The core of the Power to Methane process is the methanation reactor where a metallic catalyst that exhibits high stability over a long time and high resistance to sintering and carbon deposition is required to promote the Sabatier reaction (Eq.(1)) [8].

$$CO_2 + 4H_2 \leftrightarrow CH_4 + 2H_2O \qquad \Delta H^0_{298} = -165.0\ \text{kJ/mol} \qquad (1)$$

Heterogeneous catalysts based on metals primordially from VIII-XI group, nickel (Ni) and ruthenium (Ru), supported over mesoporous alumina ($\gamma$-$Al_2O_3$) have been found to be competitive for the

methane production by $CO_2$ methanation process. Ru-based catalysts are typically synthetized using a low metal loading (≤5 wt.%), whereas Ni-based catalysts are fabricated using a high metal loading (≤20 wt.%) [9]. Between both, Ni-based catalysts are preferred to be developed at industrial levels because of their excellent catalytic performance, easy availability, and low price. However, they are easily deactivated by sintering [10], coke deposition [11] or poisoning [12–15], in a higher extension than Ru-based catalysts [16,17], which in turn are much more expensive.

The influence of the support material ($SiO_2$ [15], $TiO_2$ [20], $Y_2O_3$ [18], $Sm_2O_3$ [11], $ZrO_2$ [23], $CeO_2$ [24], $La_2O_3$ [25], MgO [26], MCM-41 [27], carbon [28], zeolites [29–32] and KIT-6 [33]), the addition of one second metallic active phase (Fe [34], Pt, Pd, Rh [35], Co [36], V[37] and Ru [35]), and the addition of a metal oxide promoter ($ZrO_2$ [40], $CeO_2$ [41], $La_2O_3$ [42,43], $Mn_2O$ [44], CaO [45], $Gd_2O_3$ [46], MIL-101 [47]) to modify conventional $\gamma$-$Al_2O_3$ support are the main catalyst design strategies applied in order to improve the catalytic performance of the Ni-based catalysts. In our most recently works, it was reported that the addition of lanthanides promoters ($CeO_2$ and $La_2O_3$) on Ni/$\gamma$-$Al_2O_3$ microspheres was beneficial to enhanced both activity and stability [48]. Moreover, we also reported that lanthanides promoters play an important role to withstand sulphur poisoning, such in the case of $CeO_2$ [49,50]. Regarding to Ru-based catalysts, the strategy of addition $CeO_2$ as promoter has been also investigated, however its promoting effect over the physicochemical properties of the Ru/$\gamma$-$Al_2O_3$ catalysts has not been clearly reported. In literature, Rynkowski et al. [51] claimed that the stabilization of Ce (III) in $CeAl_2O_3$, which is a driving force enhancing $CO_2$ activation, is promoted by a high temperature catalyst reduction (T<900 ºC). However, taking into consideration that most of the reactor designs that are nowadays available in the market cannot operate at this high temperature reduction condition and that a stable catalyst is mandatory to carry out an industrial $CO_2$ methanation process, further research about scalable $CeO_2$ promoted Ni- and Ru- based catalysts should be conducted to clarify the $CeO_2$ promoter effects and to compare the catalytic performance between both catalytic systems at industrial levels.

In literature, the comparison and characterization of catalysts is usually performed at small lab-scale reactors whose operating conditions are easy to manage and fully controlled. Moreover, most of the reported catalyst are fabricated in powder shape with a particle size lower than 200 μm [52]. At industrial levels, powder catalysts are not technical feasible to be used in the conventional fixed-bed reactors because their small particle sizes promote the pressure drop across the catalyst bed. The use of relatively large particles (1-3 mm) can be required to avoid high pressure drop. Commercial methanation catalysts are currently manufactured in spherical (3-6 mm) [53], cylindrical (5.4x3.6 mm) [54] and ring (5x2.5 mm) [55] shapes, which are not compatible for the new generation of micro- and mm-fixed bed reactors. Therefore, the design of active catalysts at industrially relevant shape is required for a proper catalyst selection in these methanation fixed-bed reactors.

The main original contribution of the present study is the comparison of nickel and ruthenium as catalyst active phase at larger scale, and the characterization of its performance in a 1 kW mm-fixed bed reactor, including the elaboration of kinetic models for this scale. The paper is divided in three main sections: Methods, Results and Process design. The Methods section provides information on the catalyst preparation, the experimental setup, the experiment design, and the elaboration of the kinetic models. The Results section shows the reduction protocol, the analysis on the temperature profile of the reactor, the comparison between mm-sized Ni and Ru active phases performance, and the study on the degradation of the catalysts after their utilization. Finally, the Process design section presents an Aspen Plus model of potential methanation plant configurations, based on the elaborated kinetics at 1 kW scale, which optimizes the operating parameters to minimize the required amount of catalyst to reach 95vol.% of $CH_4$ in the final gas.

# 2. Methods

## 2.1. Catalyst preparation

Two mm-sized catalyst with spherical shape were considered in this work based on different active phase, nickel (Ni) and ruthenium (Ru). Both catalysts, Ni and Ru, were promoted by cerium oxide ($CeO_2$) and supported on γ-alumina spheres (dp=2-2.2 mm). Catalyst composition was selected according to preliminary works on Ni- [56] and Ru-based catalyst promoted by $CeO_2$ [57].

The catalyst preparation is described as follows. A typical synthesis consisted on 50 g-catalyst batch. The salt precursors; nickel (II) nitrate hexahydrate [$Ni(NO_3)_2 \cdot 6H_2O$] (98% purity, Alfa Aesar), or ruthenium (III) chloride hydrate [$RuCl3 \cdot xH_2O$] (Sigma-Aldrich), and cerium (III) nitrate hexahydrate [$Ce(NO_3)_2 \cdot 6H_2O$] (99% purity, Alfa Aesar) were dissolved in a rotary evaporator at constant stirring (140 rpm) for 1 hour at 120 ºC. Then, pre-dried γ-$Al_2O_3$ spheres (SA 62240, Norpro Saint-Gobain) were added to the solution and kept for 3 h for impregnation. Catalyst were calcined at 450 ºC for 30 min (1 $ºC \cdot min^{-1}$).

## 2.2. Catalyst characterization

Physiochemical characterization of the fresh and used catalysts included Scanning Electron microscopy (SEM), Energy dispersive X-ray (EDX), Helium pycnometry, Hydrogen temperature programed reduction ($H_2$-TPR), Nitrogen physisorption, X-ray diffraction (XRD) and CO-chemisorption. Prior to measurements, fresh catalysts were activated on a tubular furnace at 300 °C for 3 h (1°C·$min^{-1}$) and under 5 vol.% $H_2$/Ar flow (100 NmL·$min^{-1}$).

SEM (Zeiss Auriga 60) was used to study the morphology of the samples, while the experimental composition was studied by EDX (Oxford Inca Energy). SEM images and EDX analysis were performed by using the procedure measurement described in [48]. The true densities of catalysts were estimated by using helium pycnometer (Ultrapyc pycnometer 1200e, Quantachrome Instruments) Experiments were performed using a large sample cell that was filled by catalyst at 75% vol. to ensure accuracy (±0.02). True density was estimated by the average of collected data points from three runs measured at 1.38 bar.

Textural analyses were carried out from the corresponding $N_2$ adsorption-desorption isotherms at -196 ºC using a static automatic volumetric apparatus (TriStar II 3020-meritics analyser). Before the measurements, the samples were degassed at 90 °C for 1 h, and then at 250 °C for 4 h. Brunauer-Emmett-Teller (BET) method was applied for calculation of the BET surface area for a relative pressure ($P \cdot P_o^{-1}$) range of 0.05-0.30. The total pore volume and the average pore size were determined by applying Barrett-Joyner-Halenda (BJH) method to the desorption branch of the isotherms at value $P \cdot P_o^{-1} = 0.999$.

$H_2$-TPR and CO-Chemisorption were carried out using an automated chemisorption analyser (Autochem HP-meritics). In the case of $H_2$-TPR measurements 70 mg of synthetized material was kept under a 12 vol.% $H_2$/Ar flow (50 NmL·$min^{-1}$), while the temperature was increased from 25 to 800 °C with a heating ramp of 10 °C·$min^{-1}$. The signal of $H_2$ consumption was detected by a thermal conductivity detector (TCD). CO-Chemisorption measurements were held at 35 °C under a 10 vol.% CO/He flow over samples (50 mg), which were pre-reduced at 300 °C under a 12 vol.% $H_2$/Ar flow (50 NmL·$min^{-1}$) for 3 h (heating ramp of 1 °C·$min^{-1}$). CO pulses were periodically introduced until full saturation of the system. Metal dispersion of the catalysts was calculated assuming a stoichiometric ratio CO/Ni and CO/Ru equal to 1, an atomic weight for Ni to 58.71 and Ru to 101.07, an atomic cross-sectional area for Ni to 0.0649 $nm^2$ and for Ru to 0.0613 $nm^2$, and a density for Ni to 8.90 g·$cm^{-3}$ and Ru to 12.2 g·$cm^{-3}$.

XRD spectra were collected on a Bruker type XRD D8 Advance A25 diffractometer (Cu Kα radiation, λ = 1.5406 Å, 40 kV, 40 mA) with a scanning range of 2Θ form 20º to 80° and step size of 0.05°/3s. The average crystal sizes of the metallic nickel, ruthenium and cerium oxide nanoparticles were derived from Scherrer's equation at the most intense peaks: 2Θ=44.55º for Ni (111), 2Θ=44.07º for

Ru (101) and, 2Θ=28.71º for $CeO_2$ (220): D=(Kλ/βCosΘ), where λ is the X-ray wavelength, β is the full width of the diffraction peak at half maximum (FWHM), and Θ is the Bragg angle.

## 2.3. Experimental setup

The methanation facility (*Figure 1*) consisted on a $CO_2$ cylinder (≥99.5% purity, Air products X50S) connected to a mass flow controller (EL-Flow Bronkhorst® model F-201CV-RAD-22-K, measuring range 0.16 – 0.80 kg/h), a $H_2$ cylinder (≥99.5 purity, Air products X50S) connected to a mass flow controller (EL-Flow Bronkhorst® model F-201AV-RAD-22-V, measuring range 0.003 – 0.15 kg/h), a ceramic heater to pre-heat the reagent mixture (≤400 ºC, custom-made by Tellsa SL), a fixed bed reactor (tube in stainless steel 310 and flanges in stainless steel 304, in-house design), three electrical resistances wrapped around the reactor (3x500 W, annealed copper, model Electricfor FFC4 T-175-E), a water condenser (custom-made Tellsa SL) and a burner to co-fire the synthetic methane with butane (custom-made Tellsa SL) [58]. For cleaning and safety purposes, the facility also included a $N_2$ entry ($N_2$ bottle ≥99.998% purity, Air products X50S).

The gas composition was analyzed before and after the methanation step using a gas analyser, which consisted on a thermal conductivity detector (Calomat 6, Siemens) for $H_2$ quantification and an infrared detector (Ultramat 23, Siemens) for $CO_2$, $CH_4$ and CO quantification. Pressure and temperature were measured with standard instrumentation at different points of the installation, and were monitored using a Labview system.

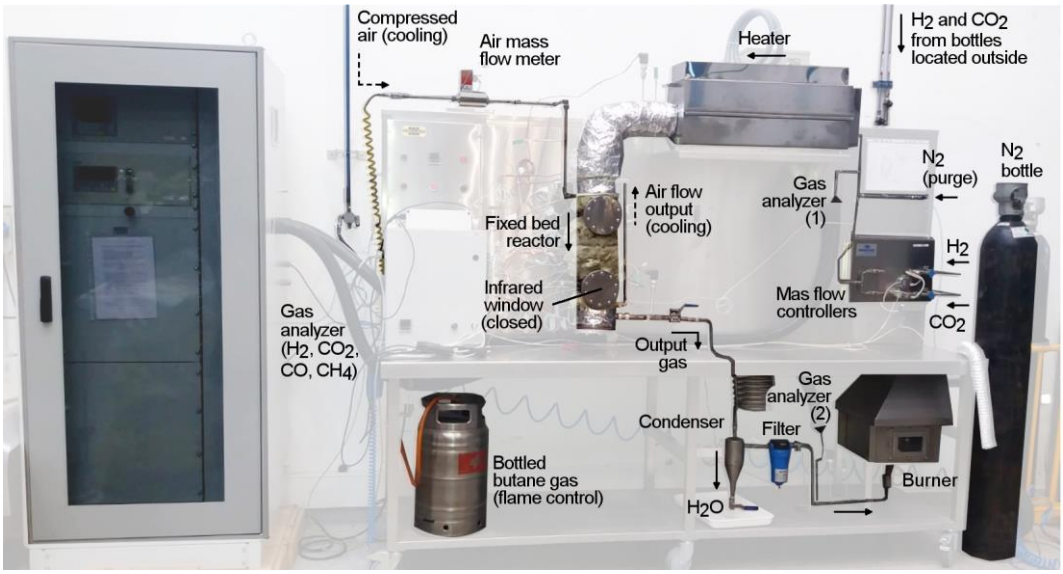


*Figure 1. Methanation test facility.*

The reactive channel consisted on a tubular fixed bed (30 mm diameter and 490 mm in length). The prepared catalyst spheres were mixed and loaded with alumina spheres (3.56 mm in diameter with a true density of 3.81 g/cm$^3$, Goodfellow AL60-SP-000122) to have a homogenous axial distribution of temperature. Additionally, two inert layers of 35 mm of alumina spheres were used to place the catalytic bed in the desired location and a 60 mm layer of quartz wool was placed at the bottom. *Table 1* describes the characteristics of the ruthenium and nickel fixed beds.

*Table 1. Physical characteristics of the fixed beds.*

| | **Ru-based** | **Ni-based** |
|---|---|---|
| Catalyst (g) | 41 | 39 |
| Inert spheres (g) | 750 | 750 |
| Total mass (g) | 791 | 789 |
| Bulk density (g/cm$^3$) | 2.285 | 2.283 |
| Void fraction (-) | 0.346 | 0.346 |

The reactor thermal design was based on a co-current "double pipe" (*Figure 2*). Air flowed through the annular space to cool the inner tube (shell of 100 mm outer diameter), while the reactants flowed through the inner tube (620 mm length and 30 mm inner diameter). A total of 9 thermocouples were distributed along the reactor length (50 mm of separation), which were placed in contact with the inner tube wall. Thus, the temperature of the wall measured by the thermocouples is expected to be representative to the actual temperature of the catalytic bed.

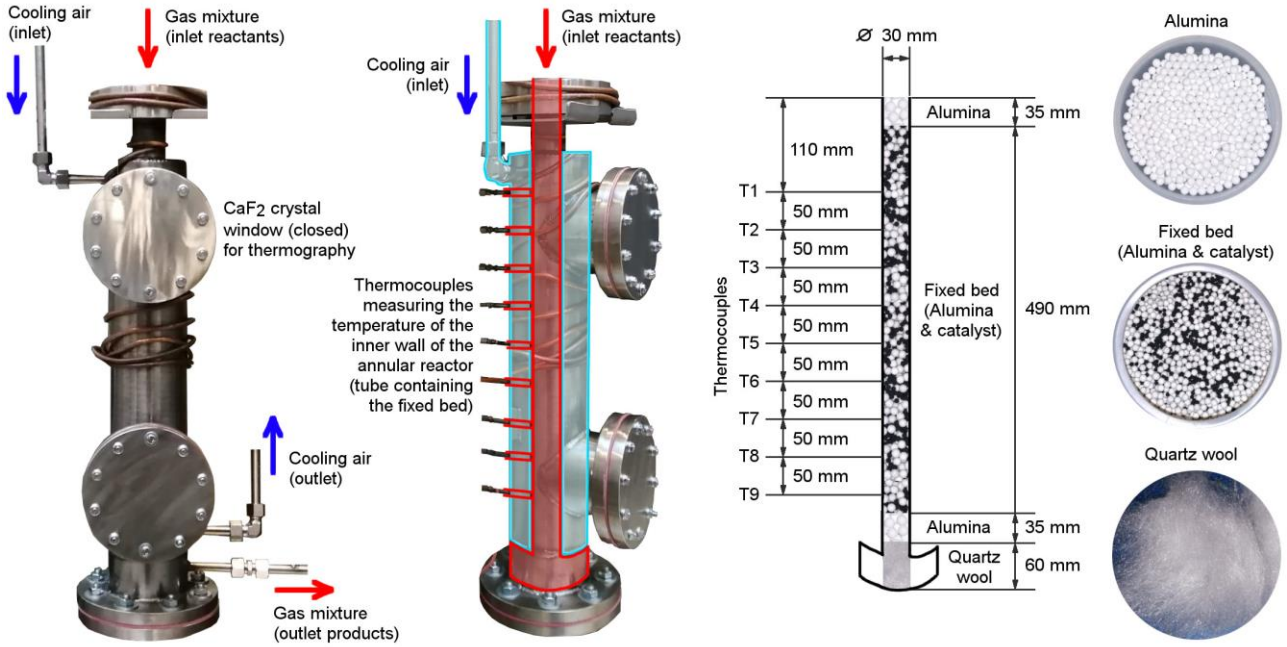


*Figure 2. Methanation reactor (without external insulation).*

## 2.4. Catalyst performance

The activation of the catalyst was carried out by passing a pure hydrogen flowrate of 0.015 kg/h during three hours at 200-400 ºC. After activation, the mass flows of $H_2$ and $CO_2$ corresponding to the operating point under study were set in the mass flow controllers. When the conversion and temperature of the reactor was stable, the measurement in the gas analyzer was recorded. The tests were performed in ascending order of operating temperature, in order to not cool the reactor between tests. When requiring increasing the temperature to reach the new operating temperature set point, the electrical resistances were set on.

The experimental plan (*Figure 3*) was designed to evaluate the performance of both catalysts at different steady conditions of operating temperature (T=250-450ºC), gas hourly space velocity (GHSV=8000-16000 $h^{-1}$), molar ratio (3.5-5.5) and activation temperature (T=200-400ºC). The operating pressure was 1 bar. The base case consisted on T=350 ºC, GHSV of 10000 $h^{-1}$ and $H_2/CO_2$ ratio of 4. The experimental design consisted of 13 independent points for each catalyst. Experiments were repeated twice for each catalyst (at different activation temperatures), therefore 52 experimental data points were measured in total. The experimental conditions of each experiments can be found at the appendixes (*Table 5* to *Table 8*).

The GHSV was calculated by Eq.(2), while the $CO_2$ conversion to $CH_4$ was experimentally calculated by Eq.(3) from the measurements of the gas analyzer:

$$GHSV = \frac{F}{m_{cat}/\rho_{cat}} \tag{2}$$

$$\eta_{CO2} = \frac{x_{CH4}}{x_{CO2} + x_{CO} + x_{CH4}} \cdot 100 \tag{3}$$

where $F$ is the volume flow of reactants (STP conditions), $m_{cat}$ the catalyst mass, $\rho_{cat}$ the bulk density of the catalyst and $x_j$ the molar fraction of component $j$ in the final gas.

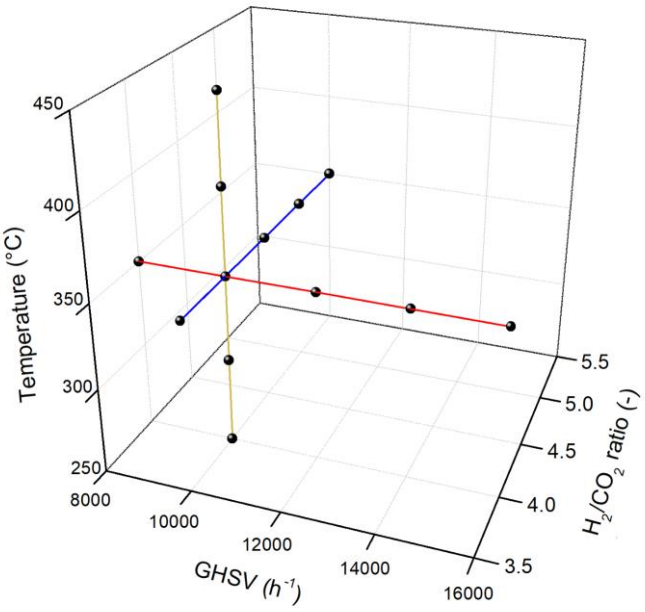


*Figure 3. Experimental design to evaluate catalyst performance. Sensitive analysis on Temperature (yellow), GHSV (red) and $H_2/CO_2$ ratio (blue).*

## 2.5. Kinetic model

A kinetic model was elaborated for each catalyst by using the experimental results of the present study. The model was based in the equation proposed by Falbo et al. (Eq. (4)) [59], which is a modification of the model reported by Lunde et al. [16].

$$r_{CO2} = \frac{k}{1 + \alpha[P_{H2O}]} \cdot \left( [P_{CO2}]^n [P_{H2}]^{4n} - \frac{[P_{CH4}]^n [P_{H2O}]^{2n}}{{K_{eq}}^n} \right) \tag{4}$$

The term $[P_i]$ is the partial pressure of component $i$, the parameter $n$ adjusts the reaction order, the coefficient $\alpha$ gives the dependence on the water partial pressure, $K_{eq}$ is the equilibrium constant (Eq.(5)), and $k$ is the rate constant (Eq.(6), Arrhenius equation).

$$K_{eq}(T) = \exp\left[ \frac{1}{1.987} \cdot \left( \frac{56000}{T^2} + \frac{34633}{T} - 16.4 \cdot ln\, T + 0.00557 \cdot T \right) + 33.165 \right] \tag{5}$$

$$k = k_0 \cdot \exp\left( -\frac{E_A}{R \cdot T} \right) \tag{6}$$

The parameters $k_0$ (pre-exponential factor), $E_A$ (activation energy), $n$ (reaction order) and $\alpha$ (dependence on water partial pressure) were obtained by minimizing the mean squared error (MSE) of the $CO_2$ conversion (Eq.(7)) over the total number $N$ of experimental tests. The MSE was minimized by using the Powell Method [60], with the following limits: 5 – 10000 mol/(s·g·atm$^{5n}$) for $k_0$, 50 – 90 kJ/mol for $E_A$, 0.001 – 1 for $n$, and 0 – 70 1/atm for $\alpha$.

$$\text{MSE} = \sqrt{\frac{\sum_j^N \left( \eta_{CO2(model),j} - \eta_{CO2(experimental),j} \right)^2}{N}} \tag{7}$$

## 2.6. Process design

The kinetic model elaborated in this study was implemented in Aspen Plus to evaluate a methanation plant able to reach a 95 vol.% of methane in the final synthetic natural gas. As case study, it was assumed an electrolysis capacity of 1 MW with 68% efficiency [61]. A conventional configuration of reactors in series with intermediate condensers was chosen (*Figure 4*).

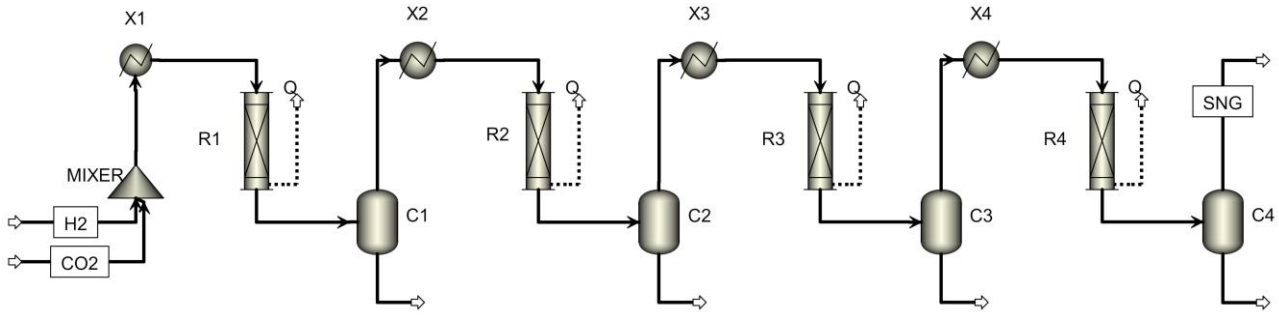


*Figure 4. Process flow diagram for the methanation plant in Aspen Plus (4-reactor configuration).*

The simulation use the RKSMHV2 property method provided by Aspen Plus. This package is based on the Redlich-Kwong-Soave equation-of-state and modified Huron-Vidal mixing rules, which are valid for the tested temperatures and pressures. An optimization process based on the Sequential Quadratic Programming (SQP) method was followed in order to minimize the amount of catalyst required, constrained by the requirement of 95vol.% $CH_4$ in the final gas. In this optimization, the temperature of the reactors and the mass of catalyst was varied, as well as the number of reactors (2, 3 or 4 reactors in series). A second optimization was performed including additional technical constrains of typical methanation plants (GHSV $\leq$ 5000 $h^{-1}$ and T $\geq$ 300 ºC [62]).

# 3. Results and discussion

## 3.1. Temperature profile along the fixed bed

During the elaboration of the kinetic model, as well as for the catalyst performance comparison, it was assumed that the reactor was isothermal. To check this condition, the temperature of the reactor was cautiously measured by 9 thermocouples spaced by 5 cm along the fixed bed (*Figure 2*). The difference of temperature with respect to the isothermal set point, in ºC, was presented in a boxplot in *Figure 5*, covering all the tests (*Table 9*). This type of graph is a standardized way of displaying data based on the minimum, the maximum, the sample median, and quartiles.

In the case of Ru-based fixed bed, the median of the temperature differences for the third to eight thermocouples was in the range +3.3% to -8.2%. Moreover, the ninth thermocouple had a median of -14.3%, which is still reasonable since its influence will be minor taking into account its proximity to the end of the fixed bed. Deviations were found for the two first thermocouples only, whose median were -25.7% and -21.3%, probably because of a loosely insulation or a bad positioning of the upper electrical resistance. Therefore, we concluded that about 70% of the length of the reactor was quasi-isothermal in practice, and the rest 30% presented small deviations with respect to the desirable set point temperature due to the scale of the reactor and the complexity of heat management. With regards to Ni-based fixed bed, the median of the temperature differences was in the range +2.2% to -11.3% accounting for all the thermocouples. Therefore, a lower temperature difference in the two first thermocouples of the tests compared to the Ru-based case. This behaviour was considered quasi-isothermal in practice.

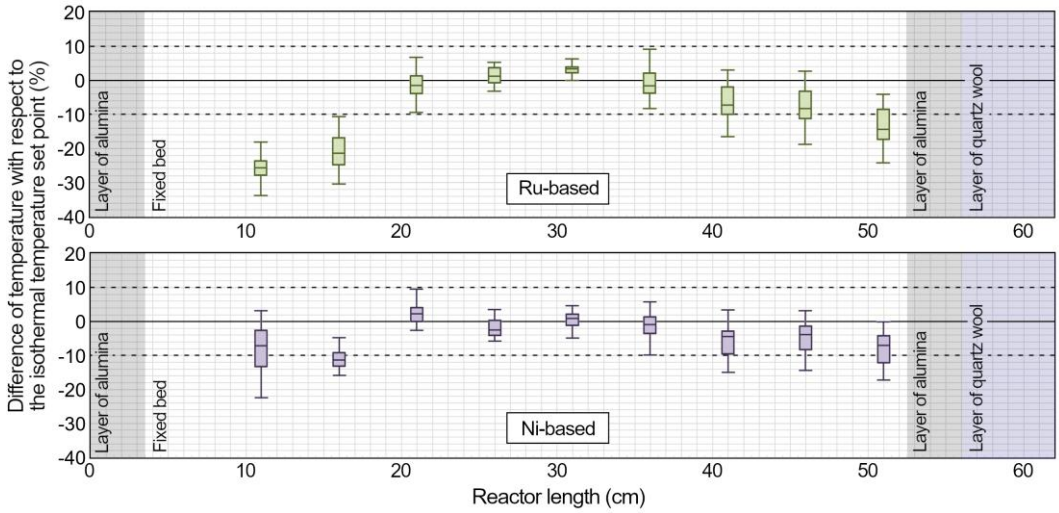


*Figure 5. Boxplot of the relative difference between the temperature (in ºC) measured along the fixed bed and the isothermal set point.*

## 3.2. Reduction protocol

The influence of the reduction temperature was evaluated for both catalysts. The obtained $CO_2$ conversion is compared through a parity plot in *Figure 6*. As it can be seen, all these points laid over the line with a slope of 1 using Ru-based. Therefore, it was concluded that there is no influence of the reduction temperature at the range of 200-300 ºC for the Ru-based catalyst. In the case of the Ni-based catalyst (activation temperatures of 300 ºC and 400 ºC), it was observed an improve in the activity for two operating points corresponding to conditions far from the equilibrium. For the rest of the operating points, at high $CO_2$ conversions, the activation temperature had no effect (points laying on the diagonal line of slope 1 in the parity plot). Since the variation in the $CO_2$ conversion with the activation procedure was negligible in most cases, an intermediate value of 300 ºC was chosen for the reduction protocol during the comparison of the catalyst performance.

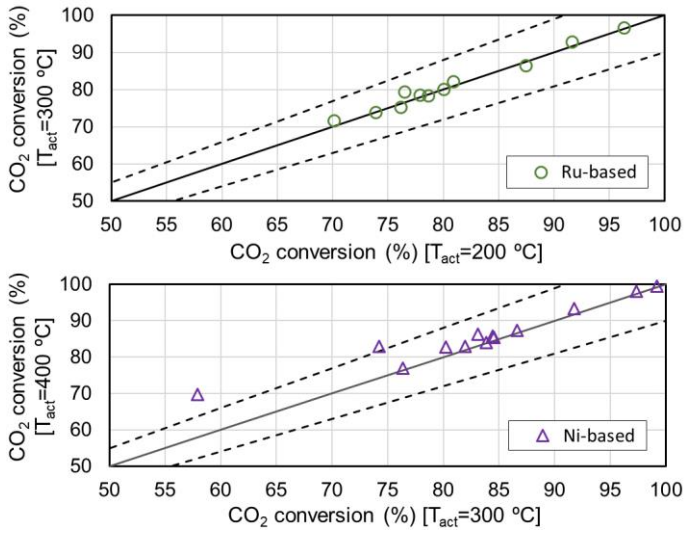


*Figure 6. Parity plot of $CO_2$ conversion at the outlet of the reactor, using different activation temperatures. The graph shows the results of Table 5, Table 6 and Table 7 versus the results of Table 8. Dashed lines show ±10% error interval.*

## 3.3. Kinetic model

The calculated parameters of the kinetic model, after the minimization of the mean squared error, are presented in *Table 2*. The mean squared error was 7.4% for the Ru-based catalyst, and 1.4% for the

Ni-based catalyst. The activation energy was 77.4 kJ/mol for the Ru-based and 69.4 kJ/mol for the Ni-based, which are in the range of the typical values found in literature (60 – 80 kJ/mol [59]).

*Table 2. Calculated kinetic parameters and minimum mean squared error.*

| | **Ru-based** | **Ni-based** |
|---|---|---|
| $k_0$ (mol/(s·g·atm$^{5n}$)) | 300.4 | 3421 |
| $E_A$ (kJ/mol) | 77.37 | 69.38 |
| $n$ (-) | 0.2397 | 0.4309 |
| $\alpha$ (1/atm) | 0.6856 | 36.22 |
| MSE (%) | 7.4 (3.0) | 1.4 |

The model results were compared to the experimental data through parity plots to validate the model (*Figure 7* and *Figure 8*). Only major deviations were found in two operating points for the Ru-based catalyst, which corresponded to the transient in which the fixed bed starts the auto-thermal behavior (between 275 and 310 ºC, Tests #Ru-T1 and #Ru-T2b, see the Appendix). If these two points are not considered when computing the MSE, we found a mean squared error of 3.0%.

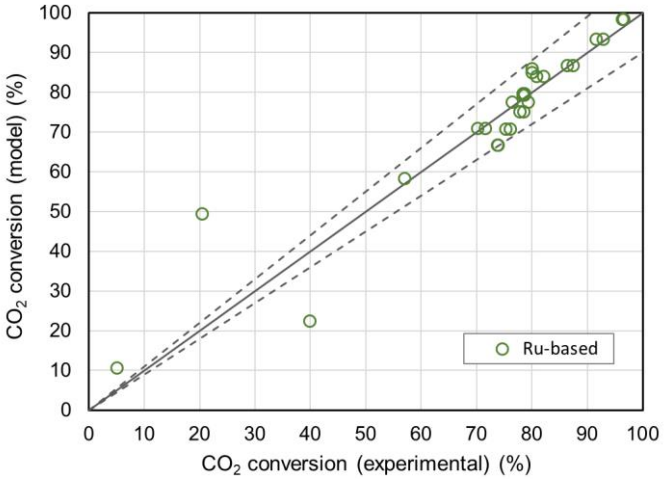


*Figure 7. Parity plot for model and experimental $CO_2$ conversion (Ru-based catalyst). Dashed lines show ±10% error interval.*

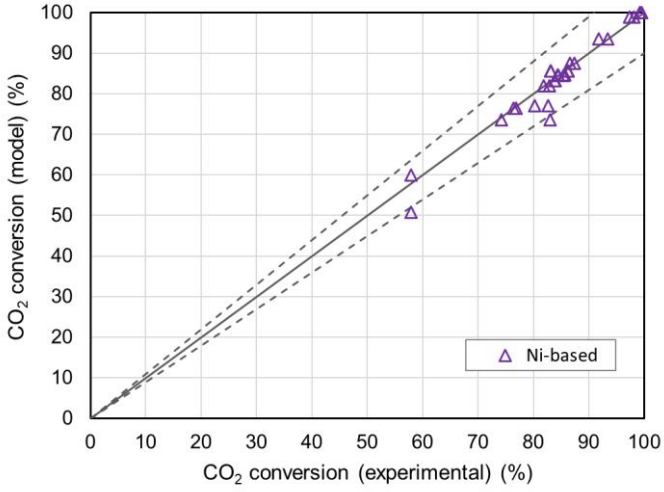


*Figure 8. Parity plot for model and experimental $CO_2$ conversion (Ni-based catalyst). Dashed lines show ±10% error interval.*

## 3.4. Catalyst performance

The influence of methanation temperature on the $CO_2$ conversion was assessed through experimental tests which make use of both catalysts activated at 300 ºC (*Table 5*). The experiments were carried out under atmospheric pressure, with a gas hourly space velocity of 10000 $h^{-1}$ and a $H_2/CO_2$ ratio equal to 4. Results illustrated in *Figure 9* follow the typical curve of a $CO_2$ methanation conversion versus temperature which may be predicted through a kinetic model. The conversion achieved with Ni-based material was higher for every tested temperature although similar conversions were reached for temperatures from 350 ºC. According to results of the kinetic model, the activity of Ni-based catalyst is about 3 times higher than the activity of Ru-based catalyst at 275 ºC, while the activity at temperatures greater than 375 ºC is nearly the same because equilibrium is reached.

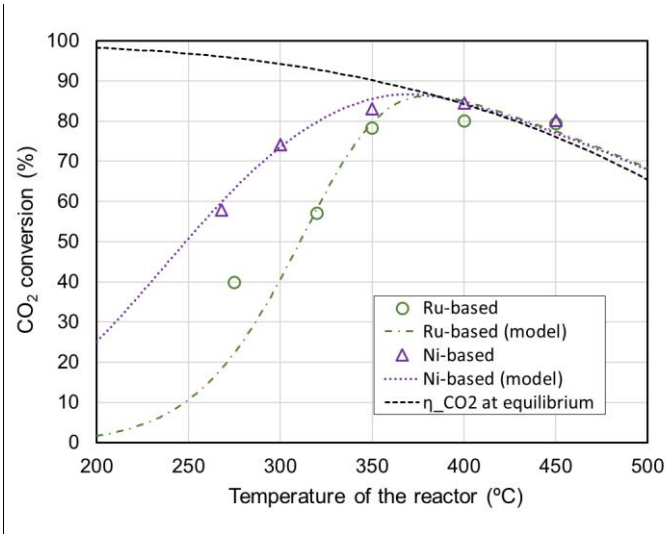


*Figure 9. $CO_2$ conversion at the outlet vs. isothermal temperature of reactor. Each point corresponds to one steady state operation. GHSV = 10000 $h^{-1}$; $H_2/CO_2$ ratio = 4; P = 1 atm (Table 5).*

The influence of gas flow was also evaluated through experimental tests carried out with both catalysts activated at 300 ºC. The experiments were performed under atmospheric pressure, with a constant temperature of 350 ºC and a $H_2/CO_2$ ratio equal to 4 (*Table 6*). The performance of Ni-based catalyst was better for every tested GHSV between 8000 and 16000 $h^{-1}$ and the trend of the experimental results for both catalysts was coherent and analogous, decreasing with the increase of the gas flowrate through the reactor (*Figure 10*). It must be highlighted that the carbon conversion obtained for a doubled flowrate (16000 $h^{-1}$) using Ni-based catalyst was similar than the conversion achieved with Ru-based catalyst (8000 $h^{-1}$). Thus, the Ni-based catalyst would allow for the treatment of a doubled gas flowrate without impact on carbon conversion. The higher GHSV, the wider difference between the conversions obtained for both catalysts.

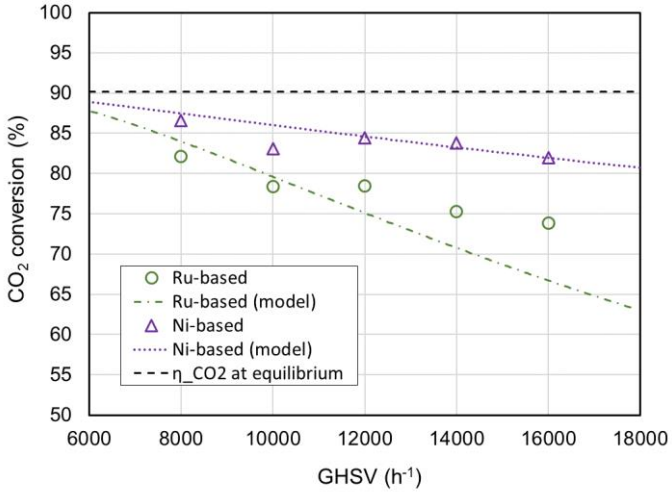


*Figure 10. $CO_2$ conversion at the outlet vs. GHSV. Each point corresponds to one steady state operation. T = 350 ºC; $H_2/CO_2$ ratio = 4; P = 1 atm (Table 6).*

The influence of increasing the $H_2/CO_2$ ratio was analyzed through experimental tests carried out with both catalysts activated at 300 ºC. The experiments were performed under atmospheric pressure, with a constant temperature of 350 ºC and a GHSV equal to 10000 $h^{-1}$ (*Table 7*). Again, the $CO_2$ conversion achieved with Ni-based catalyst were higher than those obtained with Ru-based catalyst. The trend shown by the experimental data is a linear increase of carbon conversion with $H_2/CO_2$ ratio until the equilibrium conditions are reached. The activity of the Ni-based catalyst was about 6% to 8% greater than the activity of Ru-based catalyst between the $H_2/CO_2$ ratios of 3.5 and 5 (*Figure 11*).

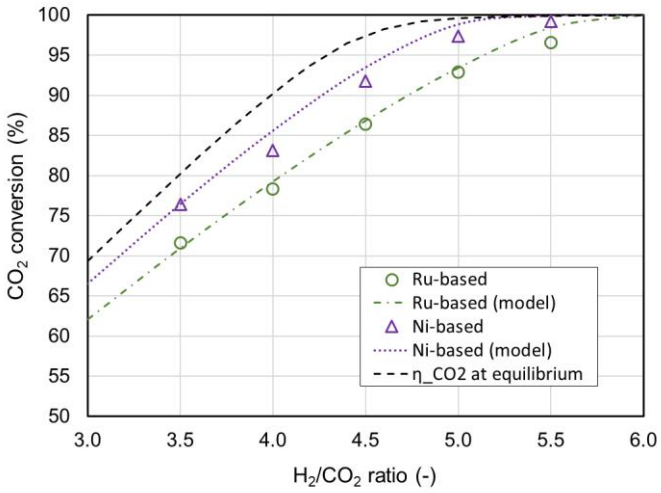


*Figure 11. $CO_2$ conversion at the outlet vs. $H_2/CO_2$ ratio at the inlet. Each point corresponds to one steady state operation. GHSV = 10000 $h^{-1}$; T = 350 ºC; P = 1 atm (Table 7).*

## 3.5. Catalyst characterization

The *Figure 12* shows $H_2$-TPR profiles of both fresh Ni- and Ru-based catalysts. In the case of the Ni-based catalyst, it was identified a small reduction peak around 225 ºC with a shoulder at 300 ºC, suggesting an interaction between $CeO_2$ and Ni. In addition, the main reduction peaks detected at around 325, 400, and 475 ºC were attributed to the reduction of NiO particles interacted weakly and strongly with the support, respectively. For the Ru-based catalyst, its main reduction peaks were identified at very low temperatures (≤150 ºC). This behaviour can be attributed to the fact that the high amount of promoter phase weakens the strong RuO-support interactions, causing over the Ru-

based catalyst a better dispersion of their metal components. For comparison purposes, the temperature of 300 ºC was selected to estimate the percentage of reducibility of the catalysts. At this conditions, Ru-based catalyst (100%) showed a higher metallic phase activation than Ni-based catalyst (13%), implying that a higher reduction temperature (≥300 ºC) can be positive to achieve the activation of Ni sites in a high percentage, as it was also identified in the experiments carried out in section 3.2. Despite the Ni-based catalyst showed a low percentage of reduction at 300 ºC, its high catalytic performance estimated in section 3.3 can be justified by the its favourable catalyst activation during the evaluation of the reaction condition parameters, as for example temperature. In this series of experiments, temperatures of 450 ºC were used, and therefore the catalyst can be activated during reaction.

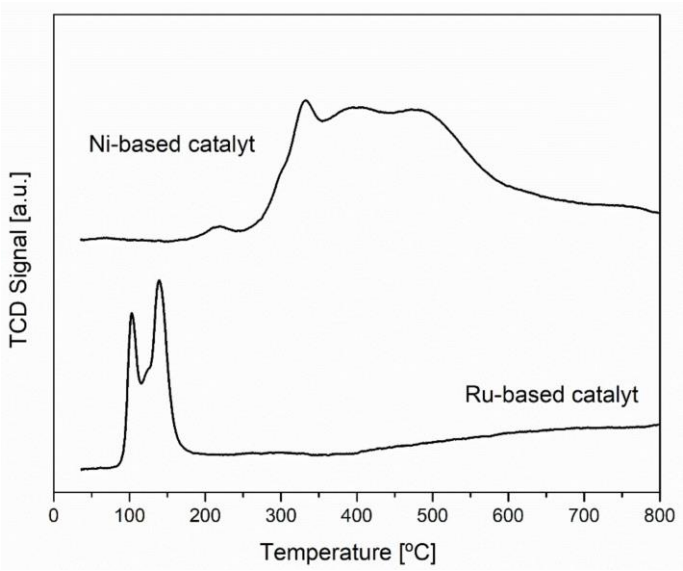


*Figure 12. $H_2$-TPR profiles of the Ni- and Ru-based catalysts*

The morphology (surface shape) and elemental composition of the Ni- and Ru-based catalyst in their two estates fresh and used were evaluated by SEM images and EDX analysis, respectively. SEM images revealed that after impregnation, both fresh Ni- (*Figure 13* (a)) and Ru-based (*Figure 14* (a)) catalyst kept the shape and mm-size of the alumina support. It was designed spherical catalysts with a verge diameter of 2.2 mm. Compared to fresh Ru-based catalyst (*Figure 14* (b)), microcracks were identified into the surface of some particles of the fresh Ni-based catalyst (see *Figure 13* (a)). The formation of small cracks into the surface can be negative since it structural phenomena can promote to the catalyst attrition by fragmentation, as it can be identified for the used Ni-based catalyst (*Figure 13* (b)). In this catalytic system, it was confirmed the breakages of the particles and particle attrition. The most probably is that during the $CO_2$ metahantion process, Ni-based particles may undergo different forces in different directions when colliding with other particles or the wall of the attrition tube, which causes fragmentation. Therefore, it can be claimed that surface features have effect on attrition resistance, and they can influence attrition mechanisms. However, it is important to note that this new microparticles had not a negative impact in the catalytic performance of the Ni-based catalyst since it showed a superior catalytic activity than that Ru-based catalyst. On the other hand, EDX analysis suggested that the experimental compositions of active and promoter phase of both catalysts, Ni-based (19.04 w.% of Ni and 13.95 wt.% of $CeO_2$) and Ru-based (2.23 w.% of Ru and 40.24 wt.% of $CeO_2$), were very close to the selected theoretical ones. In the case of the used samples, it was determined a slight reduction of the active phase. The reduction for Ni-based catalyst was 3%, while for the Ru-based catalyst was 8%. Concerning the promoter phase, an opposite behaviour was observed in the used samples. For the used Ni-based catalyst, the $CeO_2$ promoter phase was reduced a 4%. In contrast, an increase in the promoter phase of 2% was determined for the Ru-based catalyst. This reduction of active and promoter phase can be attributed to the attrition particles, A summary of the elemental composition of the two samples in their different estates is summarized in *Table 3*.

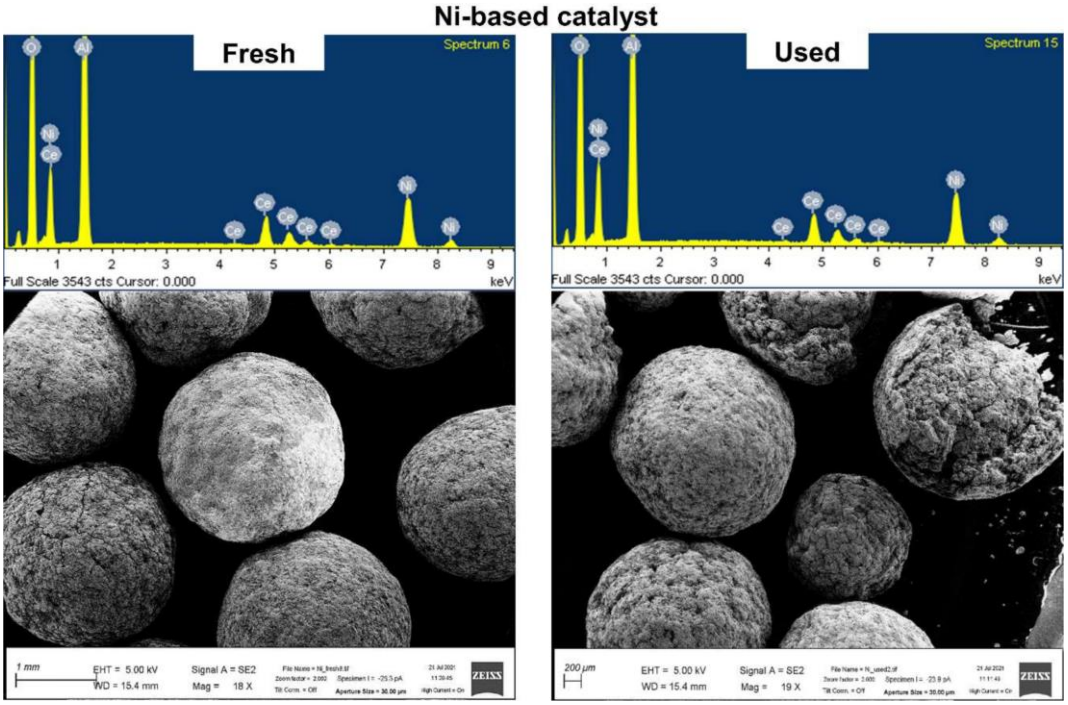


*Figure 13. SEM images of the a) fresh and b) used Ni-based catalyst*

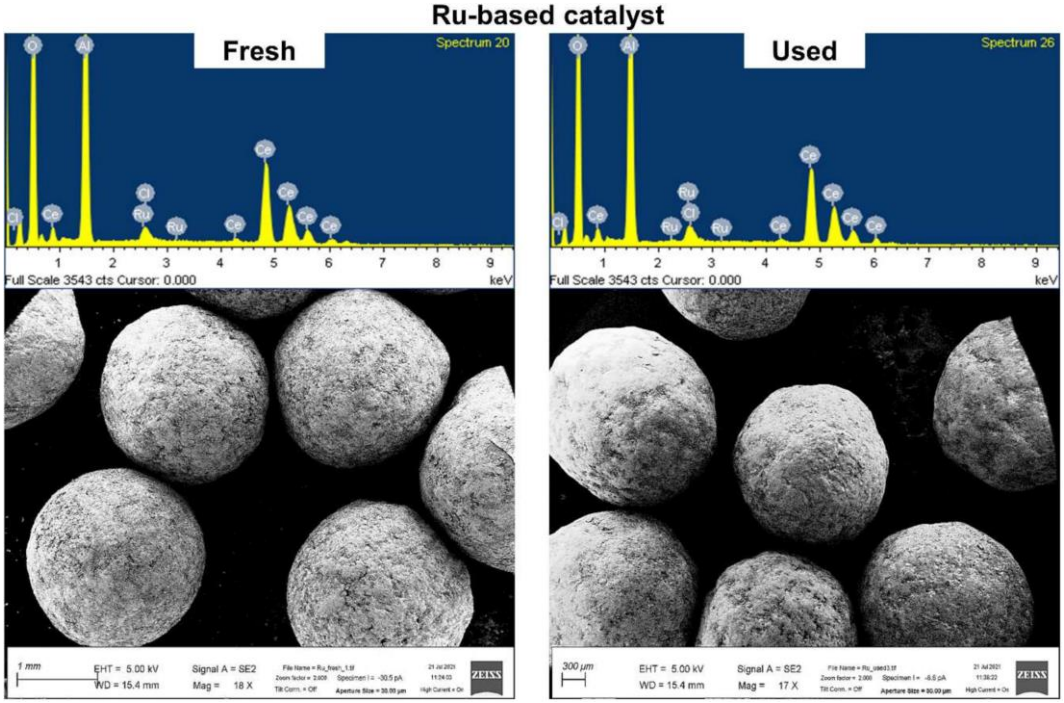


*Figure 14. SEM images of a) fresh and b) used Ru-based catalyst*

*Table 3. Physico-chemical properties of Ni- and Ru-based catalysts*

| **Property** | **Ni-based** | | **Ru-based** | |
|---|---|---|---|---|
| State | Fresh | Used | Fresh | Used |
| Elemental composition (wt%) | | | | |
| Ni | 19.04 | 18.56 | - | - |
| Ru | - | - | 2.23 | 2.06 |
| $CeO_2$ | 3.75 | 13.41 | 40.24 | 41.07 |
| Shape | Spherical | Spherical | Spherical | Spherical |
| Average Diameter (mm) | 2.2 | 2.2 | 2.2 | 2.2 |
| Density ($g/cm^3$) | 1.33 | - | 1.39 | - |
| True density ($g/cm^3$) | 3.75 | - | 3.94 | - |
| Metallic phase reduced (%) | 13 | - | 100 | - |
| BET ($m^2/g$) | 132 | 126 | 122 | 103 |
| Pore volume ($cm^3/g$) | 0.34 | 0.35 | 0.29 | 0.28 |
| Pore diameter (nm) | 9.25 | 9.17 | 9.12 | 9.47 |
| Metal dispersion (%) | 0.21 | 0.14 | 2.89 | 1.63 |
| XRD | | | | |
| dNi (nm) | 24.55 | 14.89 | - | - |
| dRu (nm) | - | - | 27.42 | 27.86 |
| $dCeO_2$ (nm) | 6.72 | 7.39 | 6.29 | 6.85 |

The *Figure 15* shows XRD patterns of both Ni-based catalyst (left) and Ru-based catalyst (right) in their fresh and used estates. At the selected temperature reduction of 300 ºC, the diffraction peaks found in the Ni-based catalysts around at 2Θ=37.24, 43.28 and 62.91º were indexed to the NiO (101), (012) and (104) lattice planes. Although the NiO phase was detected on both catalysts, these peaks were weaker in the used sample, suggesting that the reduction of the Ni-based catalyst was carried out even during the reaction. This fact can be also confirmed with the behaviour of the peaks diffraction associated with the Ni (111), (200), and (220) lattice planes identified at 2Θ=44.50, 51.84, and 76.37º, respectively. As it can be observed, the peaks of the Ni phase detected in the used catalyst were stronger than those identified in the fresh catalyst. With regard to $CeO_2$ phase, diffraction peaks at 2Θ=28.55, 33.07, and 47.49º were related to the (111), (200), (220), and (222) lattice planes. Between fresh and used catalysts, slight alterations in the intensity of the diffraction peaks were distinguished, implying mainly sintering of the $CeO_2$ particles. Regarding to Ru-based catalysts, for the fresh catalyst, the diffraction peaks identified at 2Θ=44.00 were linked to Ru (101) lattice plane. Similar to Ni-based catalyst, a diffraction peak associated with the $Al_2O_3$ (214) lattice plane was detected at 2Θ=66.52º. Besides Ru and $Al_2O_3$, $CeO_2$ (111), (200), (311), (222), (400) and (331) lattice planes were recorded at 2Θ=28.55, 33.08, 47.47, 56.33, 69.40 and 76.7º, respectively. Between fresh and used Ru-based catalysts, slight alterations in the intensity of the diffraction peaks were distinguished, implying sintering of the Ru and $CeO_2$ particles. According to XRD analysis, Ni-based catalyst shown competitive structural properties in comparison with Ru-based catalyst. After reaction, the average crystal size of the metallic nickel was 14.84 nm, whereas the metallic ruthenium was 27.86 nm. However, an opposite behaviour was observed in the average particle size of $CeO_2$. The average particle size was of approximately 7.39 nm for Ni-based catalyst and 6.85 nm for Ru-based catalyst.

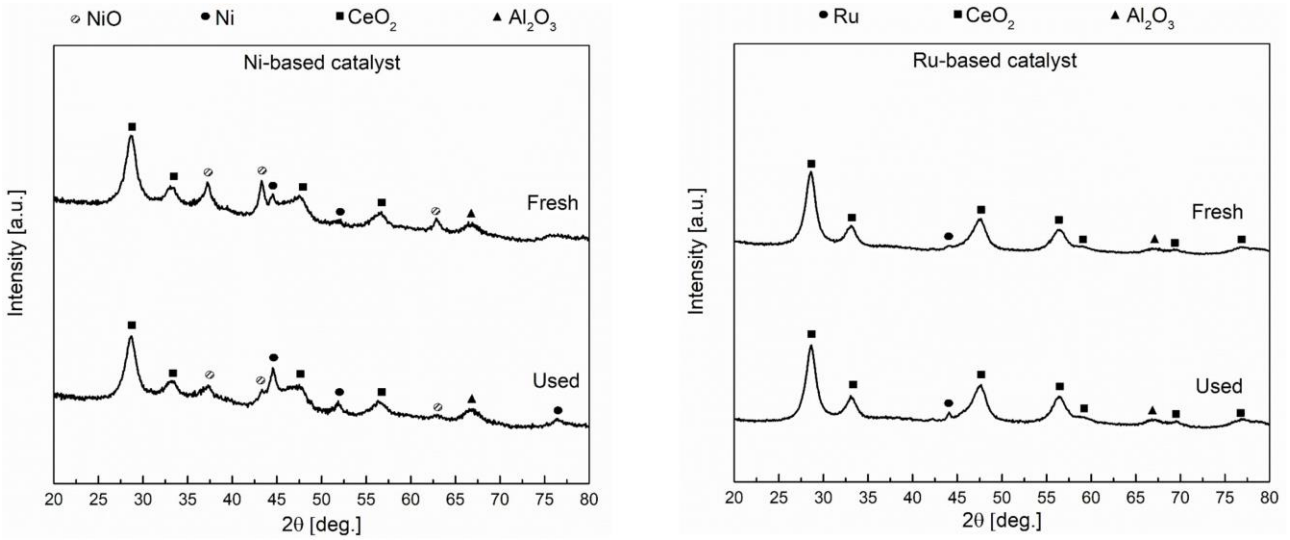


*Figure 15. Left: XRD profile of the Ni-based catalyst. [○] NiO: (101), (012) and (104); [●] Ni: (111), (200) and (220); [■] $CeO_2$: (111), (200), (220) and (222); [▲] γ-$Al_2O_3$: (214). Right: XRD profile of the Ru-based catalyst. [●] Ru: (101); [■] CeO2: ((111), (200), (311), (222), (400) and (331); [▲] γ-$Al_2O_3$: (214).*

Other structural properties, such as metal dispersion and metallic surface area of Ni- and Ru-based catalysts in their two states were also evaluated and estimated by means of CO-Chemisorption data. According to the results summarized in *Table 3*, between both fresh catalysts, the better structural properties were measured in the fresh Ru-based catalyst. These enhanced structural effects were in concordance with Ru reducibility (100%), as estimated by $H_2$-TPR measurements. Compared to fresh Ru-based catalyst (2.89% and 10.54 $m^2/g$), a metal dispersion of 0.21% and metal surface area of 1.43 $m^2/g$ were achieved for the fresh Ni-based catalyst. After the reaction, a reduction in the structural properties of both catalysts was detected. For the case of the used Ni-based catalyst, its metal dispersion is reduced to 0.14% and its metallic surface area decreased to 0.95 $m^2/g$. Concerning the used Ru-based catalysts, their structural properties were reduced by 43%. It was determined a metal dispersion of 1.63 % and metallic surface area of 5.96 $m^2/g$. These results can be linked to the increase of $CeO_2$ particles, as estimated by XRD measurements.

The nitrogen isotherms obtained for Ni-based and Ru-based catalysts were type IV of IUPAC classification, exhibiting H1 hysteresis loops with correspond to mesoporous solids. The main textural properties, such as BET surface area, pore volume and average pore diameter for both catalysts are displayed in *Table 3*. In overall, Ni-based catalyst shown the best textural properties compared to Ru-based catalyst. As can be observed, BET surface area of fresh Ni-based sample was 132 $m^2/g$, while decreased to 126 $m^2/g$ for used Ni-based sample. With regard to its other textural properties, compared to the fresh sample, an increase of 3% in the pore volume and a reduction of 1% in the pore diameter were measured for the used sample. In the case of the fresh Ru-based catalysts, its BET surface area was 122 $m^2/g$, and even lower than the fresh Ni-based catalyst. This behaviour can be mainly attributed to the high amount of $CeO_2$ promoter. After the reaction, this property decreased to 103 $m^2/g$. Compared to the used Ni-based catalyst, an opposite behaviour was detected in the pore volume and pore diameter of the used Ru-catalyst. The pore volume was reduced by 1%, while the pore diameter increased by 4%. In concordance with SEM, XRD and CO-chemisorption analysis, the modification of the textural properties in the used samples can be mainly attributed to the attrition problems detected for Ni-based catalysts and the thermal degradation of $CeO_2$ particles identified for Ru-based catalysts.

Catalytic performance test showed that the Ni-based catalyst was more active. Characterization techniques revealed that Ru-based catalyst was beneficial as active catalyst at low temperatures. However, this catalytic system showed a low catalytic activity, especially with reaction temperatures

below 350 ºC. From this temperatures, both catalysts shown similar catalytic activities; however, it was revealed that after reaction, the physicochemical properties of Ni-based catalyst were more stable than the ones Ru-based catalysts. Therefore, considering the favourable catalytic performance and the competitive physicochemical properties achieved over the $CeO_2$ promoted Ni-based catalyst makes it catalytic system promising for industrial applications.

## 3.6. Process design

After comparing the performance of both catalyst, the Ni-based catalyst was selected as the best option for evaluating a process design. It presented higher $CO_2$ conversion under all tested conditions, as well as lower decrease of BET and metal dispersion during operation. Thus, its kinetic model was implemented in Aspen Plus to analyse a methanation plant (*Figure 4*). An optimization process was followed to minimize the amount of catalyst required, constrained by the requirement of 95vol.% $CH_4$ in the final gas (independent variables: temperature and mass of catalyst in each reactor, and number of reactors). Cases #2, #3 and #4 of *Table 4* correspond to configuration of 2, 3 or 4 reactors in series. The optimization was also performed with additional technical constrains typical for large scale plants (GHSV $\leq$ 5000 $h^{-1}$ and T $\geq$ 300 ºC [62]), corresponding to cases #2C, #3C and #4C.

When no technical restrictions were included, the total mass of catalyst required in a 3-reactor plant was almost a quarter of the catalyst required when only 2 reactors were used (*Figure 16*). However, including a fourth reactor allowed diminishing the catalyst mass only by an additional 10% (with respect to the 2-reactor configuration). Moreover, the 4-reactor plant required a 26% more energy for the preheating of the gases than the 3-reactor configuration (*Figure 17*), and would lead to greater economic costs due to the additional equipment. Thus, 3 was the number of reactors that provided the best results at first approach (using low temperatures of reaction and high GHSV).

When technical restrictions were considered, 95vol.% of $CH_4$ in the final gas could not be achieved in a 2-reactor configuration (temperatures below 300 ºC would be required). The difference between the 3-reactor plant and the 4-reactor plant was similar to the previous case. The mass of catalyst was diminished by 27%, but the preheating consumption increased by 20%. This save in the mass of catalyst cannot justify increasing the cost with additional equipment and extra energy consumption. The problem in this case came from the limitation of the GHSV at 5000 $h^{-1}$, which prevented from further diminishing the amount of catalyst mass. In the 4-reactor plant, the two first reactors were at the upper limit of GHSV, and the third one close to it, so the minimization of the mass of catalyst gets remarkably constrained when 4 or more reactors are installed.

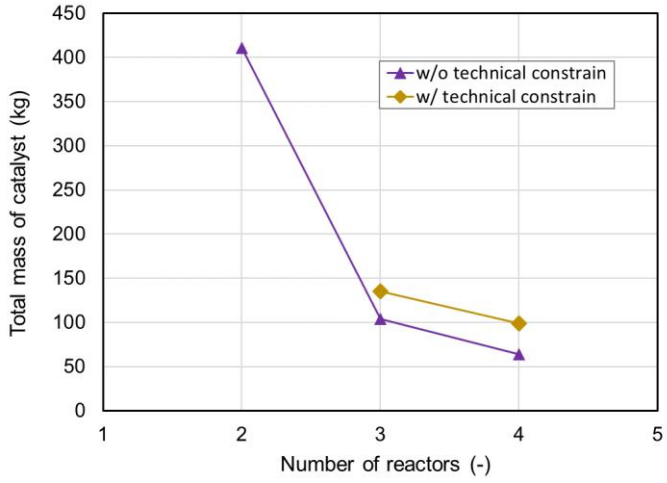


*Figure 16. Minimum total mass of Ni-based catalyst necessary to reach 95vol.% of $CH_4$ in the SNG vs. number of reactors in the methanation plant (1 MW electrolysis capacity) with and without technical constrains.*

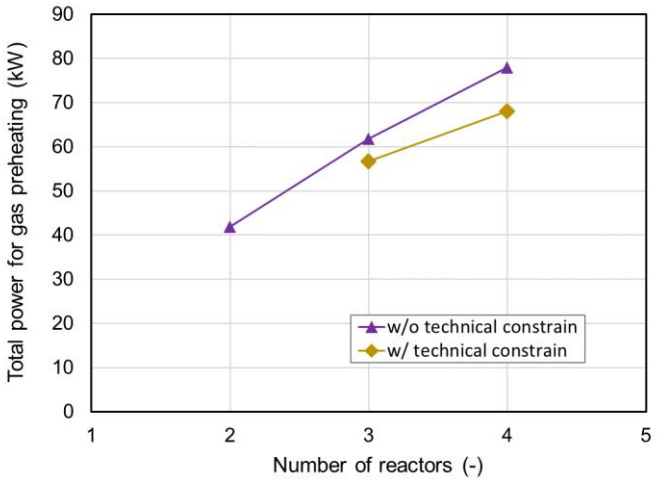


*Figure 17. Total power required for gas preheating vs. number of reactors in the methanation plant (1 MW electrolysis capacity) with and without technical constrains. The results correspond to the operation with the minimum total mass of Ni-based catalyst necessary to reach 95vol.% of $CH_4$ in the SNG.*

Thus, the 3-reactor plant was found to be the most adequate configuration when considering isothermal fixed-bed reactors operating with the Ni-based catalyst studied in this paper. In this configuration, the total amount of catalyst was 3.26 kg per kg/h of SNG produced, the preheating requirement was 4.90 MJ/$kg_{SNG}$, and the heat evacuated in the reactors was 10.8 MJ/$kg_{SNG}$. The preheating needs could be partially satisfied with the heat removed from the reactors and condensers. The average temperature of the three isothermal reactors was 320 ºC (300 – 348 ºC), and the GHSV varied from 1150 to 5000 $h^{-1}$, which is in total agreement with literature [62]. The $CO_2$ conversion in the first reactor was 90%, in the second 80% and in the third one 53%, leading to a SNG with $CH_4$ content of 95vol.%. The required electrolysis power capacity was 86.4 MJ/$kg_{SNG}$.

*Table 4. Operating parameters of the studied configurations for the methanation plant. Each configuration corresponds to an optimization that minimizes the required amount of catalyst mass.*

| **Configuration** | **#2** | **#2C** | **#3** | **#3C** | **#4** | **#4C** |
|---|---|---|---|---|---|---|
| Electrolysis capacity (MW) | 1.0 | 1.0 | 1.0 | 1.0 | 1.0 | 1.0 |
| $m_{H2}$ (kg/h) | 20.42 | 20.42 | 20.42 | 20.42 | 20.42 | 20.42 |
| $m_{CO2}$ (kg/h) | 111.45 | 111.45 | 111.45 | 111.45 | 111.45 | 111.45 |
| Pressure (atm) | 1 | 1 | 1 | 1 | 1 | 1 |
| Number of reactors | 2 | 2 | 3 | 3 | 4 | 4 |
| Type of catalyst | Ni-based | Ni-based | Ni-based | Ni-based | Ni-based | Ni-based |
| Technical constrains | | | | | | |
| - GHSV ($h^{-1}$) | - | ≤ 5000 | - | ≤ 5000 | - | ≤ 5000 |
| - T (ºC) | - | ≥ 300 | - | ≥ 300 | - | ≥ 300 |
| - $CH_4$ in SNG (vol.% dry) | 95.0 | 95.0 | 95.0 | 95.0 | 95.0 | 95.0 |
| - Condensers (ºC) | 35.0 | 35.0 | 35.0 | 35.0 | 35.0 | 35.0 |
| Reactor 1 | | | | | | |
| - T (ºC) | 320.0 | - | 380.5 | 348.0 | 411.9 | 351.8 |
| - $m_{cat}$ (kg) | 152.7 | - | 17.5 | 48.8 | 7.3 | 48.8 |
| - GHSV ($h^{-1}$) | 1598.6 | - | 13938 | 5000.0 | 33461 | 5000.0 |
| - $CO_2$ conversion (%) | 92.5 | - | 85.7 | 89.4 | 81.6 | 89.4 |
| - $CH_4$ in outlet gas (vol.% dry) | 71.1 | - | 54.4 | 62.8 | 46.9 | 62.8 |
| - Cooling (kW) | 116.1 | - | 108.9 | 113.0 | 104.4 | 113.0 |

| | | | | | | |
|---|---|---|---|---|---|---|
| Reactor 2 | | | | | | |
| - T (ºC) | 266.3 | - | 325.9 | 310.7 | 351.8 | 334.6 |
| - $m_{cat}$ (kg) | 258.5 | - | 25.1 | 37.7 | 10.8 | 14.7 |
| - GHSV ($h^{-1}$) | 260.1 | - | 3240.8 | 1955.6 | 8326.8 | 5000 |
| - $CO_2$ conversion (%) | 86.3 | - | 79.4 | 79.5 | 75.9 | 73.3 |
| - $CH_4$ in outlet gas (vol.% dry) | 95.0 | $\leq$ 94.0 | 86.7 | 89.9 | 81.1 | 87.2 |
| - Cooling (kW) | 8.0 | - | 14.3 | 10.6 | 17.6 | 9.7 |
| Reactor 3 | | | | | | |
| - T (ºC) | - | - | 285.2 | 300.0 | 311.8 | 318.1 |
| - $m_{cat}$ (kg) | - | - | 61.7 | 49.0 | 21.5 | 11.8 |
| - GHSV ($h^{-1}$) | - | - | 938.1 | 1149.0 | 2827.9 | 4881.9 |
| - $CO_2$ conversion (%) | - | - | 65.5 | 53.2 | 63.9 | 45.9 |
| - $CH_4$ in outlet gas (vol.% dry) | - | - | 95.0 | 95.0 | 92.3 | 92.7 |
| - Cooling (kW) | - | - | 2.4 | 1.4 | 3.5 | 1.6 |
| Reactor 4 | | | | | | |
| - T (ºC) | - | - | - | - | 293.6 | 300.0 |
| - $m_{cat}$ (kg) | - | - | - | - | 24.4 | 23.5 |
| - GHSV ($h^{-1}$) | - | - | - | - | 2258.0 | 2338.9 |
| - $CO_2$ conversion (%) | - | - | - | - | 36.6 | 33.2 |
| - $CH_4$ in outlet gas (vol.% dry) | - | - | - | - | 95.0 | 95.0 |
| - Cooling (kW) | - | - | - | - | 0.7 | 0.6 |
| Total cooling at reactor (kW) | 124.1 | - | 125.6 | 125.0 | 126.3 | 125.0 |
| Total cooling at condensers (kW) | 90.5 | - | 109.0 | 104.6 | 124.4 | 115.7 |
| Total preheating (kW) | 41.9 | - | 61.8 | 56.7 | 77.9 | 68.0 |
| Total $m_{cat}$ – optimization variable (kg) | 411.2 | No solution | 104.3 | 135.5 | 64.0 | 98.8 |

# 5. Conclusions

In this paper, we compared nickel and ruthenium as catalyst active phase for synthetic natural gas production at a 1 kW reactor, using in-house catalysts with ceria as promoter. The catalysts were tested in a fixed-bed reactor with bottled $CO_2$ and $H_2$. The fixed bed was 49 cm in length and 3 cm in diameter. The catalyst spheres were mixed with alumina spheres to have a homogenous distribution of temperature, which was monitored with 9 thermocouples distributed along the reactor length. The tested conditions were 250 – 450 ºC at intervals of 50 ºC, gas hourly space velocities from 8000 to 16000 $h^{-1}$ spaced by 2000 $h^{-1}$, and $H_2/CO_2$ ratios in the range 3.5 – 5.5 by steps of 0.5. All the experiments were performed at atmospheric pressure. The following conclusions were found:

- The behaviour of the reactor was considered isothermal in practice (considering the size of the reactor): The median of the difference between the measured temperature and the isothermal set point temperature was in the range +2.2% to -11.3% for the Ni-based catalyst (accounting for all the thermocouples and tests). In the case of the Ru-based catalyst, the median was between +3.3% to -14.3% for 7 out of 9 thermocouples, with variations smaller than -26% for the other two thermocouples.
- The Ni-based catalyst presented higher $CO_2$ conversion under all tested conditions: The activity of Ni-based catalyst is 3 times higher than the activity of Ru-based catalyst at 275 ºC, while the activity at temperatures greater than 375 ºC is nearly the same because equilibrium is reached.
- The Ni-based catalyst is the preferred option in terms of physicochemical properties for this reactor: The decrease of the BET and metal dispersion in Ni-based catalyst was lower than for the Ru-based catalyst.
- Two kinetic models were successfully elaborated: The models are valid for the catalysts studied in this paper and for the type of reactor used. The minimum mean squared error

between the kinetic model and the experimental measurements was 3.0% for the Ru-based catalyst and 1.4% for the Ni-based catalyst.

- In terms of plant design, the 3-reactor plant was found to be the most adequate configuration: Different potential designs of a methanation plant were evaluated in Aspen Plus for the Ni-based catalyst. The designs considered 2 to 4 reactors in series with intermediate condensers. The simulation was optimized using the SQP method in order to minimize the amount of catalyst required to reach 95vol.% of $CH_4$ in the final gas within proper technical limits ($GHSV \leq 5000$ $h^{-1}$ and temperature $\geq 300$ ºC). In the case of the 3-reactor plant, the total amount of catalyst was 3.26 kg per kg/h of SNG produced. The total useful heat removed from the reactors was 10.8 $MJ/kg_{SNG}$, while the preheating necessity was 4.90 $MJ/kg_{SNG}$. The temperature of the reactors was in the range 300 to 348 ºC, and the GHSV varied between 1150 and 5000 $h^{-1}$. The required electrolysis energy consumption was 86.4 $MJ/kg_{SNG}$. In the case of a 2-reactor plant, the 95vol.% of $CH_4$ could not be achieved in the final gas, while in the 4-reactor plant, the decrease in the required catalyst mass (-27%) does not justify the increment in preheating necessities (+20%) and the additional costs of a 4$^{th}$ reactor.

# Acknowledgments

The work described in this paper is supported by the R+D Spanish National Program from Ministerio de Economía y Competitividad, MINECO (Spanish Ministry of Economy and Competitiveness) and the European Regional Development Funds (European Commission), under project ENE2016-76850-R. This work has also been supported by the Government of Aragon (Research Group DGA T46_17R) and co-financed by FEDER 2014-2020 "Construyendo Europa desde Aragón" (ALEN OXY-PtG). This project has received funding from the European Union's Framework Programme for Research and Innovation Horizon 2020 (2014-2020) under the Marie Skłodowska-Curie Grant Agreement No. 887077. IREC is grateful to Producte19 project (AGAUR, 2019 PROD 00091) for catalyst development activities. Authors would like to acknowledge the use of "Servicio General de Apoyo a la Investigación-SAI", Universidad de Zaragoza.

# Author Contributions

Conceptualization, M.B., P.L., B.P., A.A., J.G., LM.R.; Methodology, M.B., B.P., A.A., J.G.; Software, M.B.; Validation, M.B., B.P., A.A., J.G.; Formal analysis, M.B., B.P., A.A., J.G.; Investigation, M.B., P.L., B.P., A.A., J.G., LM.R., J.P.; Writing – original draft, M.B., P.L., A.A., J.G.; Visualization, M.B., A.A., J.G.; Funding acquisition, M.B., P.L., B.P., LM.R. All authors have read and agreed to the published version of the manuscript.

# Nomenclature

**Symbols**

| | | | |
|---|---|---|---|
| $E_A$ | activation energy, kJ/mol | MSE | mean squared error, % |
| $F$ | volumetric flow (STP), $cm^3/h$ | $n$ | calculation parameter indicating the reaction order, - |
| $GHSV$ | gas hourly space velocity, 1/h | $N$ | number of experimental tests, - |
| $k_0$ | pre-exponential factor, $kmol/(s \cdot g_{cat} \cdot atm^{5n})$ | $R$ | ideal gas constant, kJ/K·mol |
| $K_{eq}$ | equilibrium constant, $1/atm^2$ | $T$ | temperature, K |
| $m$ | mass, g | $x$ | molar fraction in the final gas, - |

**Greek symbols**

| | | | |
|---|---|---|---|
| $\alpha$ | calculation parameter, 1/atm | $\rho$ | bulk density, $g/cm^3$ |
| $\eta_{CO2}$ | $CO_2$ conversion to $CH_4$, % | | |

**Subscripts and superscripts**

| | |
|---|---|
| *cat* | catalyst |

# Appendix – Experimental data

*Table 5. Experimental data for the comparison of catalyst performance under different operating temperatures.*

| Test | Fixed bed | Reduction T (ºC) | Reduction $m_{H2}$ (kg/h) | $m_{H2}$ (kg/h) | $m_{CO2}$ (kg/h) | T (ºC) | GHSV ($h^{-1}$) | $H_2/CO_2$ (-) | $\eta_{CO2}$ (%) | $\eta_{CO2}$ (%) at equil. | $CH_4$ (%vol. dry) | $CO_2$ (%vol. dry) | CO (%vol. dry) | $H_2$ (%vol. dry) |
|---|---|---|---|---|---|---|---|---|---|---|---|---|---|---|
| #Ru-T1 | Ru | 300 | 0.015 | 0.03241 | 0.17827 | 275 | 10,000 | 4.0 | 39.9 | 95.7 | 13.0 | 19.6 | 0.0 | 69.6 |
| #Ru-T2 | Ru | 300 | 0.015 | 0.03241 | 0.17827 | 320 | 10,000 | 4.0 | 57.0 | 92.9 | 23.0 | 17.3 | 0.0 | 60.0 |
| #Ru-T3 | Ru | 300 | 0.015 | 0.03241 | 0.17827 | 350 | 10,000 | 4.0 | 78.4 | 90.2 | 44.7 | 12.3 | 0.1 | 42.3 |
| #Ru-T4 | Ru | 300 | 0.015 | 0.03241 | 0.17827 | 400 | 10,000 | 4.0 | 80.0 | 84.3 | 47.0 | 11.7 | 0.1 | 40.5 |
| #Ru-T5 | Ru | 300 | 0.015 | 0.03241 | 0.17827 | 450 | 10,000 | 4.0 | 79.4 | 76.1 | 46.2 | 11.8 | 0.2 | 41.4 |
| #Ni-T1 | Ni | 300 | 0.015 | 0.03204 | 0.17623 | 268 | 10,000 | 4.0 | 57.9 | 95.7 | 23.5 | 17.0 | 0.1 | 60.3 |
| #Ni-T2 | Ni | 300 | 0.015 | 0.03204 | 0.17623 | 300 | 10,000 | 4.0 | 74.2 | 92.9 | 38.7 | 13.4 | 0.1 | 46.9 |
| #Ni-T3 | Ni | 300 | 0.015 | 0.03204 | 0.17623 | 350 | 10,000 | 4.0 | 83.1 | 90.2 | 52.2 | 10.5 | 0.1 | 36.2 |
| #Ni-T4 | Ni | 300 | 0.015 | 0.03204 | 0.17623 | 400 | 10,000 | 4.0 | 84.5 | 84.3 | 54.2 | 9.8 | 0.1 | 34.8 |
| #Ni-T5 | Ni | 300 | 0.015 | 0.03204 | 0.17623 | 450 | 10,000 | 4.0 | 80.2 | 76.1 | 47.9 | 11.5 | 0.3 | 40.5 |

*Table 6. Experimental data for the comparison of catalyst performance under different GHSV.*

| Test | Fixed bed | Reduction T (ºC) | Reduction $m_{H2}$ (kg/h) | $m_{H2}$ (kg/h) | $m_{CO2}$ (kg/h) | T (ºC) | GHSV ($h^{-1}$) | $H_2/CO_2$ (-) | $\eta_{CO2}$ (%) | $\eta_{CO2}$ (%) at equil. | $CH_4$ (%vol. dry) | $CO_2$ (%vol. dry) | CO (%vol. dry) | $H_2$ (%vol. dry) |
|---|---|---|---|---|---|---|---|---|---|---|---|---|---|---|
| #Ru-G1 | Ru | 300 | 0.015 | 0.02593 | 0.14262 | 350 | 8,000 | 4.0 | 82.1 | 90.3 | 49.7 | 10.8 | 0.1 | 36.6 |
| #Ru-G2 | Ru | 300 | 0.015 | 0.03241 | 0.17827 | 350 | 10,000 | 4.0 | 78.4 | 90.3 | 44.7 | 12.3 | 0.1 | 42.3 |
| #Ru-G3 | Ru | 300 | 0.015 | 0.03890 | 0.21393 | 350 | 12,000 | 4.0 | 78.5 | 90.3 | 44.8 | 12.2 | 0.1 | 42.3 |
| #Ru-G4 | Ru | 300 | 0.015 | 0.04538 | 0.24958 | 350 | 14,000 | 4.0 | 75.3 | 90.3 | 40.1 | 13.0 | 0.1 | 46.5 |
| #Ru-G5 | Ru | 300 | 0.015 | 0.05186 | 0.28524 | 350 | 16,000 | 4.0 | 73.8 | 90.3 | 38.2 | 13.4 | 0.2 | 48.4 |
| #Ni-G1 | Ni | 300 | 0.015 | 0.02563 | 0.14098 | 350 | 8,000 | 4.0 | 86.6 | 90.3 | 60.0 | 9.2 | 0.1 | 30.0 |
| #Ni-G2 | Ni | 300 | 0.015 | 0.03204 | 0.17623 | 350 | 10,000 | 4.0 | 83.1 | 90.3 | 52.2 | 10.5 | 0.1 | 36.2 |
| #Ni-G3 | Ni | 300 | 0.015 | 0.03845 | 0.21147 | 350 | 12,000 | 4.0 | 84.4 | 90.3 | 55.2 | 10.1 | 0.1 | 34.4 |
| #Ni-G4 | Ni | 300 | 0.015 | 0.04486 | 0.24672 | 350 | 14,000 | 4.0 | 83.8 | 90.3 | 53.3 | 10.2 | 0.1 | 36.2 |
| #Ni-G5 | Ni | 300 | 0.015 | 0.05127 | 0.28197 | 350 | 16,000 | 4.0 | 81.9 | 90.3 | 50.5 | 11.0 | 0.1 | 39.1 |

*Table 7. Experimental data for the comparison of catalyst performance under different $H_2/CO_2$ ratios.*

| Test | Fixed bed | Reduction T (ºC) | Reduction $m_{H2}$ (kg/h) | $m_{H2}$ (kg/h) | $m_{CO2}$ (kg/h) | T (ºC) | GHSV ($h^{-1}$) | $H_2/CO_2$ (-) | $\eta_{CO2}$ (%) | $\eta_{CO2}$ (%) at equil. | $CH_4$ (%vol. dry) | $CO_2$ (%vol. dry) | CO (%vol. dry) | $H_2$ (%vol. dry) |
|---|---|---|---|---|---|---|---|---|---|---|---|---|---|---|
| #Ru-R1 | Ru | 300 | 0.015 | 0.03151 | 0.19808 | 350 | 10,000 | 3.5 | 71.6 | 80.3 | 46.7 | 18.4 | 0.1 | 34.0 |
| #Ru-R2 | Ru | 300 | 0.015 | 0.03241 | 0.17827 | 350 | 10,000 | 4.0 | 78.4 | 90.3 | 44.7 | 12.3 | 0.1 | 42.3 |
| #Ru-R3 | Ru | 300 | 0.015 | 0.03315 | 0.16207 | 350 | 10,000 | 4.5 | 86.4 | 97.4 | 44.1 | 6.9 | 0.0 | 47.9 |
| #Ru-R4 | Ru | 300 | 0.015 | 0.03376 | 0.14856 | 350 | 10,000 | 5.0 | 92.9 | 99.6 | 42.5 | 3.2 | 0.0 | 53.4 |
| #Ru-R5 | Ru | 300 | 0.015 | 0.03428 | 0.13713 | 350 | 10,000 | 5.5 | 96.6 | 99.9 | 38.0 | 1.4 | 0.0 | 60.0 |
| #Ni-R1 | Ni | 300 | 0.015 | 0.03115 | 0.19581 | 350 | 10,000 | 3.5 | 76.4 | 80.3 | 56.7 | 17.4 | 0.1 | 25.9 |
| #Ni-R2 | Ni | 300 | 0.015 | 0.03204 | 0.17623 | 350 | 10,000 | 4.0 | 83.1 | 90.3 | 52.2 | 10.5 | 0.1 | 36.2 |
| #Ni-R3 | Ni | 300 | 0.015 | 0.03277 | 0.16021 | 350 | 10,000 | 4.5 | 91.8 | 97.4 | 54.6 | 4.9 | 0.0 | 40.4 |
| #Ni-R4 | Ni | 300 | 0.015 | 0.03338 | 0.14686 | 350 | 10,000 | 5.0 | 97.3 | 99.6 | 47.3 | 1.3 | 0.0 | 56.6 |
| #Ni-R5 | Ni | 300 | 0.015 | 0.03389 | 0.13556 | 350 | 10,000 | 5.5 | 99.2 | 99.9 | 40.1 | 0.3 | 0.0 | 59.2 |

*Table 8. Repetition of experimental data of Table 5, Table 6 and Table 7 at different reduction temperature.*

| Test | Fixed bed | Reduction | | $m_{H2}$ (kg/h) | $m_{CO2}$ (kg/h) | T (ºC) | GHSV ($h^{-1}$) | $H_2/CO_2$ (-) | $\eta_{CO2}$ (%) | $\eta_{CO2}$ (%) at equil. | $CH_4$ | $CO_2$ | CO | $H_2$ |
|---|---|---|---|---|---|---|---|---|---|---|---|---|---|---|
| | | T (ºC) | $m_{H2}$ (kg/h) | | | | | | | | (%vol. dry) | | | |
| #Ru-T1b | Ru | 200 | 0.015 | 0.03241 | 0.17827 | 250 | 10,000 | 4.0 | 5.1 | 95.7 | 1.2 | 22.2 | 0.0 | 79.7 |
| #Ru-T2b | Ru | 200 | 0.015 | 0.03241 | 0.17827 | 310 | 10,000 | 4.0 | 20.5 | 92.9 | 5.5 | 21.3 | 0.0 | 76.0 |
| #Ru-T3b | Ru | 200 | 0.015 | 0.03241 | 0.17827 | 350 | 10,000 | 4.0 | 78.6 | 90.2 | 45.0 | 12.1 | 0.1 | 42.0 |
| #Ru-T4b | Ru | 200 | 0.015 | 0.03241 | 0.17827 | 390 | 10,000 | 4.0 | 80.1 | 84.3 | 48.6 | 11.9 | 0.2 | 39.3 |
| #Ru-T5b | Ru | 200 | 0.015 | 0.03241 | 0.17827 | 450 | 10,000 | 4.0 | 76.5 | 76.1 | 40.4 | 12.2 | 0.2 | 42.3 |
| #Ru-G1b | Ru | 200 | 0.015 | 0.02593 | 0.14262 | 350 | 8,000 | 4.0 | 80.9 | 90.3 | 48.6 | 11.4 | 0.1 | 38.8 |
| #Ru-G2b | Ru | 200 | 0.015 | 0.03241 | 0.17827 | 350 | 10,000 | 4.0 | 78.6 | 90.3 | 45.0 | 12.1 | 0.1 | 42.0 |
| #Ru-G3b | Ru | 200 | 0.015 | 0.03890 | 0.21393 | 350 | 12,000 | 4.0 | 77.9 | 90.3 | 44.0 | 12.4 | 0.1 | 43.0 |
| #Ru-G4b | Ru | 200 | 0.015 | 0.04538 | 0.24958 | 350 | 14,000 | 4.0 | 76.1 | 90.3 | 41.8 | 12.9 | 0.1 | 45.4 |
| #Ru-G5b | Ru | 200 | 0.015 | 0.05186 | 0.28524 | 350 | 16,000 | 4.0 | 73.9 | 90.3 | 39.5 | 13.8 | 0.1 | 47.7 |
| #Ru-R1b | Ru | 200 | 0.015 | 0.03151 | 0.19808 | 350 | 10,000 | 3.5 | 70.2 | 80.3 | 43.6 | 18.4 | 0.2 | 36.5 |
| #Ru-R2b | Ru | 200 | 0.015 | 0.03241 | 0.17827 | 350 | 10,000 | 4.0 | 78.6 | 90.3 | 45.0 | 12.1 | 0.1 | 42.0 |
| #Ru-R3b | Ru | 200 | 0.015 | 0.03315 | 0.16207 | 350 | 10,000 | 4.5 | 87.5 | 97.4 | 46.3 | 6.6 | 0.1 | 46.4 |
| #Ru-R4b | Ru | 200 | 0.015 | 0.03376 | 0.14856 | 350 | 10,000 | 5.0 | 91.6 | 99.6 | 40.9 | 3.7 | 0.0 | 54.6 |
| #Ru-R5b | Ru | 200 | 0.015 | 0.03428 | 0.13713 | 350 | 10,000 | 5.5 | 96.3 | 99.9 | 38.2 | 1.5 | 0.0 | 60.0 |
| #Ni-T1b | Ni | 400 | 0.015 | 0.03204 | 0.17623 | 250 | 10,000 | 4.0 | 57.9 | 95.7 | 21.9 | 15.9 | 0.1 | 57.9 |
| #Ni-T2b | Ni | 400 | 0.015 | 0.03204 | 0.17623 | 300 | 10,000 | 4.0 | 83.0 | 92.9 | 49.4 | 10.1 | 0.0 | 34.6 |
| #Ni-T3b | Ni | 400 | 0.015 | 0.03204 | 0.17623 | 350 | 10,000 | 4.0 | 86.2 | 90.2 | 55.5 | 8.9 | 0.0 | 30.1 |
| #Ni-T4b | Ni | 400 | 0.015 | 0.03204 | 0.17623 | 400 | 10,000 | 4.0 | 85.4 | 84.3 | 54.7 | 9.3 | 0.1 | 31.0 |
| #Ni-T5b | Ni | 400 | 0.015 | 0.03204 | 0.17623 | 450 | 10,000 | 4.0 | 82.7 | 76.1 | 50.0 | 10.3 | 0.1 | 35.2 |
| #Ni-G1b | Ni | 400 | 0.015 | 0.02563 | 0.14098 | 350 | 8,000 | 4.0 | 87.4 | 90.3 | 59.0 | 8.5 | 0.0 | 27.2 |
| #Ni-G2b | Ni | 400 | 0.015 | 0.03204 | 0.17623 | 350 | 10,000 | 4.0 | 86.2 | 90.3 | 55.5 | 8.9 | 0.0 | 30.1 |
| #Ni-G3b | Ni | 400 | 0.015 | 0.03845 | 0.21147 | 350 | 12,000 | 4.0 | 85.7 | 90.3 | 54.2 | 9.0 | 0.1 | 31.7 |
| #Ni-G4b | Ni | 400 | 0.015 | 0.04486 | 0.24672 | 350 | 14,000 | 4.0 | 83.9 | 90.3 | 51.5 | 9.8 | 0.1 | 34.4 |
| #Ni-G5b | Ni | 400 | 0.015 | 0.05127 | 0.28197 | 350 | 16,000 | 4.0 | 82.9 | 90.3 | 49.1 | 10.0 | 0.1 | 36.4 |
| #Ni-R1b | Ni | 400 | 0.015 | 0.03115 | 0.19581 | 350 | 10,000 | 3.5 | 76.9 | 80.3 | 55.7 | 16.7 | 0.1 | 22.6 |
| #Ni-R2b | Ni | 400 | 0.015 | 0.03204 | 0.17623 | 350 | 10,000 | 4.0 | 86.2 | 90.3 | 55.5 | 8.9 | 0.0 | 30.1 |
| #Ni-R3b | Ni | 400 | 0.015 | 0.03277 | 0.16021 | 350 | 10,000 | 4.5 | 93.4 | 97.4 | 51.9 | 3.7 | 0.0 | 39.3 |
| #Ni-R4b | Ni | 400 | 0.015 | 0.03338 | 0.14686 | 350 | 10,000 | 5.0 | 98.1 | 99.6 | 43.8 | 0.9 | 0.0 | 50.4 |
| #Ni-R5b | Ni | 400 | 0.015 | 0.03389 | 0.13556 | 350 | 10,000 | 5.5 | 99.6 | 99.9 | 36.0 | 0.2 | 0.0 | 59.6 |

*Table 9. Temperatures (ºC) measured at the wall of the tube containing the fixed bed.*

| *Test* | *Set point (ºC)* | *1* | *2* | *3* | *4* | *5* | *6* | *7* | *8* | *9* |
|---|---|---|---|---|---|---|---|---|---|---|
| #Ru-T1 | 275 | 225.2 | 231.0 | 258.2 | 272.2 | 285.5 | 270.2 | 254.9 | 249.9 | 231.9 |
| #Ru-T2 | 320 | 246.7 | 271.4 | 292.0 | 309.7 | 328.0 | 320.9 | 304.9 | 295.5 | 274.9 |
| #Ru-T3 | 350 | 260.7 | 276.5 | 324.2 | 347.0 | 353.6 | 336.5 | 315.4 | 307.0 | 283.7 |
| #Ru-T4 | 400 | 264.9 | 313.0 | 396.2 | 407.9 | 406.4 | 378.6 | 345.6 | 335.8 | 3136 |
| #Ru-T5 | 450 | 326.8 | 374.5 | 443.2 | 451.6 | 449.7 | 421.1 | 390.9 | 372.3 | 341.0 |
| #Ru-T1b | 250 | 223.9 | 242.4 | 248.9 | 259.8 | 258.4 | 264.7 | 245.1 | 242.7 | 230.6 |
| #Ru-T2b | 310 | 261.4 | 299.4 | 310.5 | 317.9 | 301.6 | 306.7 | 274.6 | 274.2 | 261.0 |
| #Ru-T3b | 350 | 266.7 | 278.3 | 339.0 | 342.7 | 367.3 | 368.5 | 352.6 | 352.7 | 335.7 |
| #Ru-T4b | 390 | 289.9 | 313.9 | 378.6 | 396.9 | 403.0 | 383.7 | 361.7 | 346.7 | 312.9 |
| #Ru-T5b | 450 | 317.6 | 374.1 | 439.8 | 447.0 | 441.5 | 412.7 | 375.9 | 365.7 | 344.1 |
| #Ru-G1 | 350 | 253.1 | 259.5 | 344.5 | 340.8 | 361.5 | 356.1 | 343.8 | 341.9 | 324.6 |
| #Ru-G2 | 350 | 260.7 | 276.5 | 324.2 | 347.0 | 353.6 | 336.5 | 315.4 | 307.0 | 283.7 |
| #Ru-G3 | 350 | 251.0 | 259.9 | 356.0 | 355.0 | 365.2 | 351.6 | 338.0 | 336.8 | 317.4 |
| #Ru-G4 | 350 | 238.7 | 249.8 | 326.5 | 347.5 | 357.2 | 337.8 | 323.8 | 320.0 | 299.2 |
| #Ru-G5 | 350 | 229.7 | 243.5 | 317.0 | 353.2 | 358.5 | 328.0 | 309.9 | 303.2 | 278.9 |
| #Ru-G1b | 350 | 286.2 | 312.9 | 355.5 | 363.1 | 371.9 | 364.8 | 344.2 | 338.4 | 319.2 |
| #Ru-G2b | 350 | 266.7 | 278.3 | 339.0 | 342.7 | 367.3 | 368.5 | 352.6 | 352.7 | 335.7 |
| #Ru-G3b | 350 | 265.4 | 274.2 | 352.6 | 347.8 | 371.2 | 363.8 | 347.3 | 347.5 | 332.3 |
| #Ru-G4b | 350 | 250.1 | 263.7 | 348.8 | 365.6 | 365.5 | 340.5 | 325.9 | 321.6 | 300.2 |
| #Ru-G5b | 350 | 260.0 | 273.6 | 373.7 | 392.2 | 404.4 | 382.1 | 360.8 | 359.3 | 334.1 |
| #Ru-R1 | 350 | 259.8 | 273.5 | 343.2 | 357.9 | 362.6 | 347.9 | 324.1 | 318.2 | 296.8 |
| #Ru-R2 | 350 | 260.7 | 276.5 | 324.2 | 347.0 | 353.6 | 336.5 | 315.4 | 307.0 | 283.7 |
| #Ru-R3 | 350 | 255.1 | 261.4 | 338.0 | 348.5 | 358.0 | 347.7 | 324.7 | 325.6 | 306.0 |
| #Ru-R4 | 350 | 254.6 | 262.5 | 354.4 | 359.4 | 361.6 | 342.7 | 320.5 | 320.8 | 299.3 |
| #Ru-R5 | 350 | 255.6 | 264.2 | 363.9 | 365.2 | 363.0 | 337.2 | 315.1 | 313.8 | 291.6 |
| #Ru-R1b | 350 | 261.1 | 270.3 | 331.7 | 339.0 | 362.5 | 362.1 | 348.4 | 349.4 | 333.9 |
| #Ru-R2b | 350 | 266.7 | 278.3 | 339.0 | 342.7 | 367.3 | 368.5 | 352.6 | 352.7 | 335.7 |
| #Ru-R3b | 350 | 265.9 | 279.2 | 356.2 | 362.8 | 361.4 | 339.9 | 327.2 | 322.7 | 302.1 |
| #Ru-R4b | 350 | 268.3 | 282.7 | 338.7 | 353.1 | 359.3 | 344.4 | 333.6 | 329.2 | 309.2 |
| #Ru-R5b | 350 | 266.8 | 279.4 | 367.8 | 368.5 | 363.3 | 336.6 | 322.1 | 317.4 | 296.7 |
| #Ni-T1 | 268 | 237.0 | 233.4 | 274.2 | 268.9 | 266.2 | 258.8 | 250.1 | 247.3 | 234.9 |
| #Ni-T2 | 300 | 236.4 | 241.1 | 299.4 | 292.8 | 313.1 | 317.4 | 310.4 | 309.5 | 299.8 |
| #Ni-T3 | 350 | 271.6 | 294.6 | 343.7 | 346.5 | 361.2 | 363.1 | 352.5 | 347.6 | 334.5 |
| #Ni-T4 | 400 | 335.9 | 360.3 | 389.8 | 401.5 | 413.5 | 421.2 | 401.3 | 399.8 | 391.0 |
| #Ni-T5 | 450 | 414.7 | 426.7 | 459.7 | 463.7 | 462.0 | 456.0 | 431.4 | 428.2 | 416.8 |
| #Ni-T1b | 250 | 238.1 | 229.4 | 260.8 | 254.6 | 253.6 | 247.0 | 242.8 | 245.6 | 241.5 |
| #Ni-T2b | 300 | 265.4 | 269.7 | 313.2 | 299.4 | 301.3 | 292.0 | 279.9 | 280.8 | 273.6 |
| #Ni-T3b | 350 | 361.1 | 330.7 | 383.3 | 356.8 | 366.3 | 358.0 | 335.9 | 341.4 | 333.6 |
| #Ni-T4b | 400 | 389.2 | 380.8 | 419.4 | 409.4 | 406.5 | 391.8 | 362.8 | 361.3 | 351.7 |
| #Ni-T5b | 450 | 428.2 | 437.1 | 464.7 | 465.8 | 454.7 | 433.7 | 398.2 | 389.4 | 375.3 |
| #Ni-G1 | 350 | 325.6 | 306.9 | 357.7 | 337.9 | 348.6 | 344.6 | 329.9 | 337.9 | 328.4 |
| #Ni-G2 | 350 | 271.6 | 294.6 | 343.7 | 346.5 | 361.2 | 363.1 | 352.5 | 347.6 | 334.5 |
| #Ni-G3 | 350 | 335.6 | 311.9 | 364.0 | 341.2 | 355.7 | 354.9 | 338.7 | 348.0 | 339.8 |
| #Ni-G4 | 350 | 303.4 | 301.1 | 350.5 | 335.4 | 352.9 | 352.3 | 341.4 | 347.4 | 339.1 |
| #Ni-G5 | 350 | 315.0 | 312.4 | 374.6 | 344.7 | 355.9 | 349.7 | 337.7 | 344.6 | 333.8 |
| #Ni-G1b | 350 | 357.9 | 314.0 | 359.4 | 338.3 | 349.1 | 345.8 | 334.8 | 334.0 | 325.6 |
| #Ni-G2b | 350 | 361.1 | 330.7 | 383.3 | 356.8 | 366.3 | 358.0 | 335.9 | 341.4 | 333.6 |
| #Ni-G3b | 350 | 342.1 | 304.6 | 348.7 | 330.0 | 332.9 | 319.5 | 303.5 | 309.9 | 300.3 |
| #Ni-G4b | 350 | 354.1 | 309.1 | 359.2 | 335.5 | 332.9 | 318.0 | 300.3 | 307.1 | 296.7 |
| #Ni-G5b | 350 | 337.0 | 304.3 | 357.4 | 331.4 | 340.8 | 334.3 | 314.0 | 322.6 | 316.0 |
| #Ni-R1 | 350 | 280.3 | 299.9 | 358.0 | 348.3 | 357.6 | 353.1 | 341.6 | 340.1 | 325.0 |
| #Ni-R2 | 350 | 271.6 | 294.6 | 343.7 | 346.5 | 361.2 | 363.1 | 352.5 | 347.6 | 334.5 |
| #Ni-R3 | 350 | 303.9 | 308.6 | 368.7 | 348.9 | 357.6 | 351.6 | 334.1 | 337.5 | 324.0 |
| #Ni-R4 | 350 | 294.4 | 295.9 | 344.3 | 335.9 | 354.6 | 356.1 | 347.7 | 350.2 | 339.9 |
| #Ni-R5 | 350 | 307.4 | 302.4 | 353.9 | 337.2 | 350.6 | 347.7 | 338.6 | 342.9 | 331.8 |
| #Ni-R1b | 350 | 324.6 | 319.3 | 355.5 | 340.2 | 336.5 | 320.3 | 303.5 | 302.8 | 294.3 |
| #Ni-R2b | 350 | 361.1 | 330.7 | 383.3 | 356.8 | 366.3 | 358.0 | 335.9 | 341.4 | 333.6 |
| #Ni-R3b | 350 | 342.8 | 317.5 | 360.8 | 338.7 | 334.7 | 315.7 | 297.7 | 299.5 | 289.9 |
| #Ni-R4b | 350 | 340.5 | 307.9 | 349.4 | 331.0 | 342.0 | 343.5 | 322.8 | 326.1 | 319.9 |
| #Ni-R5b | 350 | 350.9 | 311.9 | 355.6 | 335.8 | 347.8 | 351.9 | 334.2 | 335.8 | 328.9 |

# References


[1] Capros P, De Vita A, Florou A, Kannavou M, Fotiou T, Siskos P, et al. EU Reference Scenario 2020. 2021. https://doi.org/10.2833/35750.

[2] Daiyan R, Macgill I, Amal R. Opportunities and Challenges for Renewable Power-to-X. ACS Energy Lett 2020;5:3843–7. https://doi.org/10.1021/acsenergylett.0c02249.

[3] Bailera M, Lisbona P, Peña B, Romeo LM. A review on CO2 mitigation in the Iron and Steel industry through Power to X processes. J CO2 Util 2021;46:101456. https://doi.org/10.1016/j.jcou.2021.101456.

[4] Bailera M, Lisbona P, Romeo LM, Espatolero S. Power to Gas projects review: Lab, pilot and demo plants for storing renewable energy and CO2. Renew Sustain Energy Rev 2017;69. https://doi.org/10.1016/j.rser.2016.11.130.

[5] Bailera M, Lisbona P. Energy storage in Spain: Forecasting electricity excess and assessment of power-to-gas potential up to 2050. Energy 2018;143. https://doi.org/10.1016/j.energy.2017.11.069.

[6] Katla D, Jurczyk M, Skorek-Osikowska A, Uchman W. Analysis of the integrated system of electrolysis and methanation units for the production of synthetic natural gas (SNG). Energy 2021;237. https://doi.org/10.1016/j.energy.2021.121479.

[7] Uchman W, Skorek-Osikowska A, Jurczyk M, Węcel D. The analysis of dynamic operation of power-to-SNG system with hydrogen generator powered with renewable energy, hydrogen storage and methanation unit. Energy 2020;213. https://doi.org/10.1016/j.energy.2020.118802.

[8] Gao J, Liu Q, Gu F, Liu B, Zhong Z, Su F. Recent advances in methanation catalysts for the production of synthetic natural gas. RSC Adv 2015;5:22759–76. https://doi.org/10.1039/c4ra16114a.

[9] Garbarino G, Bellotti D, Riani P, Magistri L, Busca G. Methanation of carbon dioxide on Ru/Al2O3 and Ni/Al2O3 catalysts at atmospheric pressure: Catalysts activation, behaviour and stability. Int J Hydrogen Energy 2015;40:9171–82. https://doi.org/10.1016/j.ijhydene.2015.05.059.

[10] Ewald S, Kolbeck M, Kratky T, Wolf M, Hinrichsen O. On the deactivation of Ni-Al catalysts in CO2 methanation. Appl Catal A Gen 2019;570:376–86. https://doi.org/10.1016/j.apcata.2018.10.033.

[11] Muroyama H, Tsuda Y, Asakoshi T, Masitah H, Okanishi T, Matsui T, et al. Carbon dioxide methanation over Ni catalysts supported on various metal oxides. J Catal 2016;343:178–84. https://doi.org/10.1016/j.jcat.2016.07.018.

[12] Wolf M, Wong LH, Schüler C, Hinrichsen O. CO2 methanation on transition-metal-promoted Ni-Al catalysts: Sulfur poisoning and the role of CO2 adsorption capacity for catalyst activity. J CO2 Util 2020;36:276–87. https://doi.org/10.1016/j.jcou.2019.10.014.

[13] Méndez-Mateos D, Barrio VL, Requies JM, Cambra JF. A study of deactivation by H2S and regeneration of a Ni catalyst supported on Al2O3, during methanation of CO2. Effect of the promoters Co, Cr, Fe and Mo. RSC Adv 2020;10:16551–64. https://doi.org/10.1039/d0ra00882f.

[14] Legras B, Ordomsky V V, Dujardin C, Virginie M, Khodakov AY. Impact and Detailed Action of Sulfur in Syngas on Methane Synthesis on Ni/γ-Al2O3 Catalyst. ACS Catal 2014;4:2785–91. https://doi.org/10.1021/cs500436f.

[15] Müller K, Fleige M, Rachow F, Schmeiber D. Sabatier based CO2-methanation of flue gas emitted by conventional power plants. Energy Procedia 2013;40:240–8.

[16] Lunde PJ, Kester FL. Rates of methane formation from carbon dioxide and hydrogen over a ruthenium catalyst. J Catal 1973;30:423–9. https://doi.org/10.1016/0021-9517(73)90159-0.

[17] Schoder M, Armbruster U, Martin A. Heterogen katalysierte Hydrierung von Kohlendioxid zu Methan unter erhohten Drucken. Chemie-Ingenieur-Technik 2013;85:344–52. https://doi.org/10.1002/cite.201200112.

[18] Wu HC, Chang YC, Wu JH, Lin JH, Lin IK, Chen CS. Methanation of CO2 and reverse water gas shift reactions on Ni/SiO2 catalysts: the influence of particle size on selectivity and reaction pathway. Catal Sci Technol 2015;5:4154–63. https://doi.org/10.1039/c5cy00667h.

[19] Zhou G, Liu H, Xing Y, Xu S, Xie H, Xiong K. CO2 hydrogenation to methane over mesoporous

Co/SiO2 catalysts: Effect of structure. J CO2 Util 2018;26:221–9. https://doi.org/10.1016/j.jcou.2018.04.023.

[20] Zhou R, Rui N, Fan Z, Liu C. Effect of the structure of Ni/TiO2 catalyst on CO2 methanation. Int J Hydrogen Energy 2016;41:22017–25. https://doi.org/10.1016/J.IJHYDENE.2016.08.093.

[21] Yan Y, Dai Y, Yang Y, Lapkin AA. Improved stability of Y2O3 supported Ni catalysts for CO2 methanation by precursor-determined metal-support interaction. Appl Catal B Environ 2018;237:504–12. https://doi.org/10.1016/j.apcatb.2018.06.021.

[22] Italianoa C, Llorcab J, Pinoa L, Ferraroa M, Antonuccia V, Vitaa A. CO and CO2 methanation over Ni catalysts supported on CeO2, Al2O3 and Y2O3 oxides. Appl Catal A Gen 2020. https://doi.org/10.7868/s0002337x13030160.

[23] Everett OE, Zonetti PC, Alves OC, de Avillez RR, Appel LG. The role of oxygen vacancies in the CO2 methanation employing Ni/ZrO2 doped with Ca. Int J Hydrogen Energy 2020;45:6352–9. https://doi.org/10.1016/j.ijhydene.2019.12.140.

[24] Winter LR, Gomez E, Yan B, Yao S, Chen JG. Tuning Ni-catalyzed CO2 hydrogenation selectivity via Ni-ceria support interactions and Ni-Fe bimetallic formation. Appl Catal B Environ 2018;224:442–50. https://doi.org/10.1016/j.apcatb.2017.10.036.

[25] Song H, Yang J, Zhao J, Chou L. Methanation of Carbon Dioxide over a Highly Dispersed Ni/La2O3 Catalyst. Chinese J Catal 2010;31:21–3. https://doi.org/10.1016/s1872-2067(09)60036-x.

[26] Yan Y, Dai Y, He H, Yu Y, Yang Y. Applied Catalysis B : Environmental A novel W-doped Ni-Mg mixed oxide catalyst for CO 2 methanation. "Applied Catal B, Environ 2016;196:108–16. https://doi.org/10.1016/j.apcatb.2016.05.016.

[27] Bacariza MC, Graça I, Bebiano SS, Lopes JM, Henriques C. Micro- and mesoporous supports for CO2 methanation catalysts: A comparison between SBA-15, MCM-41 and USY zeolite. Chem Eng Sci 2018;175:72–83. https://doi.org/10.1016/j.ces.2017.09.027.

[28] Romero-Sáez M, Dongil AB, Benito N, Espinoza-González R, Escalona N, Gracia F. CO2 methanation over nickel-ZrO2 catalyst supported on carbon nanotubes: A comparison between two impregnation strategies. Appl Catal B Environ 2018;237:817–25. https://doi.org/10.1016/j.apcatb.2018.06.045.

[29] Graça I, González L V., Bacariza MC, Fernandes A, Henriques C, Lopes JM, et al. CO2 hydrogenation into CH4 on NiHNaUSY zeolites. Appl Catal B Environ 2014;147:101–10. https://doi.org/10.1016/j.apcatb.2013.08.010.

[30] Zhang W, Machida H, Takano H, Izumiya K, Norinaga K. Computational fluid dynamics simulation of CO2 methanation in a shell-and-tube reactor with multi-region conjugate heat transfer. Chem Eng Sci 2020;211:115276. https://doi.org/10.1016/j.ces.2019.115276.

[31] Czuma N, Zarębska K, Motak M, Gálvez ME, Da Costa P. Ni/zeolite X derived from fly ash as catalysts for CO2 methanation. Fuel 2020;267. https://doi.org/10.1016/j.fuel.2020.117139.

[32] Bacariza MC, Bértolo R, Graça I, Lopes JM, Henriques C. The effect of the compensating cation on the catalytic performances of Ni/USY zeolites towards CO2 methanation. J CO2 Util 2017;21:280–91. https://doi.org/10.1016/j.jcou.2017.07.020.

[33] Cao H, Wang W, Cui T, Wang H, Zhu G, Ren X. Enhancing CO2 hydrogenation to methane by Ni-based catalyst with V species using 3D-mesoporous KIT-6 as support. Energies 2020;13. https://doi.org/10.3390/en13092235.

[34] Pandey D, Deo G. Effect of support on the catalytic activity of supported Ni–Fe catalysts for the CO2 methanation reaction. J Ind Eng Chem 2016;33:99–107. https://doi.org/10.1016/j.jiec.2015.09.019.

[35] Mihet M, Lazar MD. Methanation of CO2 on Ni/γ-Al2O3: Influence of Pt, Pd or Rh promotion. Catal Today 2018;306:294–9. https://doi.org/10.1016/j.cattod.2016.12.001.

[36] Xu L, Lian X, Chen M, Cui Y, Wang F, Li W, et al. CO2 methanation over Co-Ni bimetal-doped ordered mesoporous Al2O3 catalysts with enhanced low-temperature activities. Int J Hydrogen Energy 2018;43:17172–84. https://doi.org/10.1016/j.ijhydene.2018.07.106.

[37] Le TA, Kim J, Kang JK, Park ED. CO and CO2 methanation over M (M[dbnd]Mn, Ce, Zr, Mg, K, Zn, or V)-promoted Ni/Al@Al2O3 catalysts. Catal Today 2019. https://doi.org/10.1016/j.cattod.2019.08.058.

[38] Chein R-Y, Wang C-C. Experimental Study on CO2 Methanation over Ni/Al2O3, Ru/Al2O3, and Ru-Ni/Al2O3 Catalysts. Catalysts 2020;10:1112. https://doi.org/10.3390/catal10101112.

[39] Zhen W, Li B, Lu G, Ma J. Enhancing catalytic activity and stability for CO2 methanation on Ni-Ru/γ-Al2O3via modulating impregnation sequence and controlling surface active species. RSC Adv 2014;4:16472–9. https://doi.org/10.1039/c3ra47982j.

[40] Zhan Y, Wang Y, Gu D, Chen C, Jiang L, Takehira K. Ni/Al2O3-ZrO2 catalyst for CO2 methanation: The role of γ-(Al, Zr)2O3 formation. Appl Surf Sci 2018;459:74–9. https://doi.org/10.1016/j.apsusc.2018.07.206.

[41] Rahmani S, Rezaei M, Meshkani F. Preparation of promoted nickel catalysts supported on mesoporous nanocrystalline gamma alumina for carbon dioxide methanation reaction. J Ind Eng Chem 2014;20:4176–82. https://doi.org/10.1016/j.jiec.2014.01.017.

[42] Rivero-Mendoza DE, Stanley JNG, Scott J, Aguey-Zinsou KF. An alumina-supported ni-la-based catalyst for producing synthetic natural gas. Catalysts 2016;6:1–15. https://doi.org/10.3390/catal6110170.

[43] Garbarino G, Wang C, Cavattoni T, Finocchio E, Riani P, Flytzani-Stephanopoulos M, et al. A study of Ni/La-Al2O3 catalysts: A competitive system for CO2 methanation. Appl Catal B Environ 2018. https://doi.org/https://doi.org/10.1016/j.apcatb.2018.12.063.

[44] Zhao K, Li Z, Bian L. CO2 methanation and co-methanation of CO and CO2 over Mn-promoted Ni/Al2O3 catalysts. Front Chem Sci Eng 2016;10:273–80. https://doi.org/10.1007/s11705-016-1563-5.

[45] Liu Q, Wang S, Zhao G, Yang H, Yuan M, An X, et al. CO2 methanation over ordered mesoporous NiRu-doped CaO-Al2O3 nanocomposites with enhanced catalytic performance. Int J Hydrogen Energy 2018;43:239–50. https://doi.org/10.1016/j.ijhydene.2017.11.052.

[46] Frontera P, Malara A, Modafferi V, Antonucci V, Antonucci P, Macario A. Catalytic activity of Ni-Co supported metals in carbon dioxides methanation . Can J Chem Eng 2020. https://doi.org/10.1002/cjce.23780.

[47] Grad O, Mihet M, Blanita G, Dan M, Barbu-Tudoran L, Lazar MD. MIL-101-Al2O3 as catalytic support in the methanation of CO2 – Comparative study between Ni/MIL-101 and Ni/MIL-101-Al2O3 catalysts. Catal Today 2020. https://doi.org/10.1016/j.cattod.2020.05.003.

[48] Guilera J, del Valle J, Alarcón A, Díaz JA, Andreu T. Metal-oxide promoted Ni/Al2O3 as CO2 methanation micro-size catalysts. J CO2 Util 2019;30:11–7. https://doi.org/https://doi.org/10.1016/j.jcou.2019.01.003.

[49] Alarcon A, Guilera J, Soto R, Andreu T. Higher tolerance to sulfur poisoning in CO2 methanation by the presence of CeO2 2019. https://doi.org/10.1016/j.apcatb.2019.118346.

[50] Guilera J, Soto R, Alarcón A, Andreu T. Satisfactory catalyst stability in SNG production using real biogas despite sulfur poisoning evidences at different reactor zones. Fuel 2021;306. https://doi.org/10.1016/j.fuel.2021.121682.

[51] Rynkowski JM, Paryjczak T, Lewicki A, Szynkowska MI, Maniecki TP, Jóźwiak WK. Characterization of Ru/CeO2-Al2O3 catalysts and their performance in CO2 methanation. React Kinet Catal Lett 2000;71:55–64. https://doi.org/10.1023/A:1010326031095.

[52] Nam H, Kim JH, Kim H, Kim MJ, Jeon SG, Jin GT, et al. CO2 methanation in a bench-scale bubbling fluidized bed reactor using Ni-based catalyst and its exothermic heat transfer analysis. Energy 2021;214:118895. https://doi.org/10.1016/j.energy.2020.118895.

[53] Clariant. METH® 134 Catalyst for methanation in ammonia or syngas production 2019.

[54] Matthey J. Methanation catalysts 2020.

[55] Topsøe H. PK-7R Pre-reduced methanation catalyst 2020.

[56] Alarcón A, Guilera J, Díaz JA, Andreu T. Optimization of nickel and ceria catalyst content for synthetic natural gas production through CO2 methanation. Fuel Process Technol 2019;193:114–22. https://doi.org/https://doi.org/10.1016/j.fuproc.2019.05.008.

[57] Martin San José C. Catalizadores de alta actividad a baja temperatura para la producción de gas natural sintéctico. Universitat de Barcelona, 2020.

[58] Bailera M, Peña B, Lisbona P, Marín J, Romeo LM. Lab-scale experimental tests of power to gas-oxycombustion hybridization: System design and preliminary results. Energy 2021;226:120375. https://doi.org/10.1016/j.energy.2021.120375.

[59] Falbo L, Martinelli M, Visconti CG, Lietti L, Bassano C, Deiana P. Kinetics of CO2methanation on a Ru-based catalyst at process conditions relevant for Power-to-Gas applications. Appl Catal B Environ 2018;225:354–63. https://doi.org/10.1016/j.apcatb.2017.11.066.

[60] Vassiliadis VS, Conejeros R. Powell Method. Encycl. Optim., Boston, MA: Springer US; 2008, p. 3012–3. https://doi.org/10.1007/978-0-387-74759-0_516.

[61] Bailera M, Lisbona P, Peña B, Romeo LM. Energy Storage. Cham: Springer International Publishing; 2020. https://doi.org/10.1007/978-3-030-46527-8.

[62] Götz M, Lefebvre J, Mörs F, McDaniel Koch A, Graf F, Bajohr S, et al. Renewable Power-to-Gas: A technological and economic review. Renew Energy 2016;85:1371–90. https://doi.org/10.1016/j.renene.2015.07.066.